CEST-MRI for body oncologic imaging: are we there yet?

Elena Vinogradov[1,2], **Jochen Keupp**[3], **Ivan E. Dimitrov**[2,4], **Stephen Seiler**[1], **Ivan Pedrosa**[1,2]

[1]Department of Radiology, University of Texas Southwestern Medical Center, Dallas, TX, USA

[2]Advanced Imaging Research Center, University of Texas Southwestern Medical Center, Dallas, TX
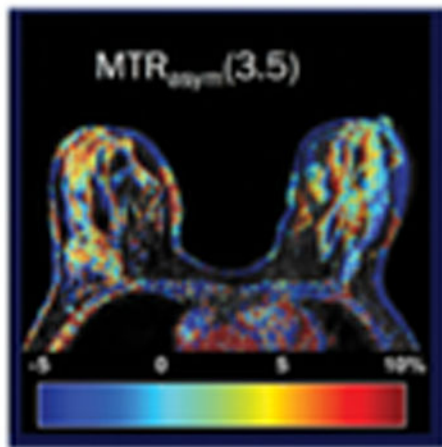
[3]Philips Research, Hamburg, Germany

[4]Philips Healthcare, Gainesville, FL, USA

Abstract

Chemical Exchange Saturation Transfer (CEST) MRI has gained recognition as a valuable addition to the molecular imaging and quantitative biomarkers arsenal, especially for characterization of brain tumors. There is also increasing interest in the use of CEST-MRI for applications beyond the brain. However, its translation to body oncology applications lags behind those in neuro-oncology. The slower migration of CEST-MRI to non-neurologic applications reflects the technical challenges inherent to imaging of the torso. In this review, we discuss the application of CEST-MRI to oncologic conditions of the breast and torso (i.e., body imaging), emphasizing the challenges and potential solutions to address them. While data are still limited, reported studies suggest that CEST signal is associated with important histology markers such as tumor grade, receptor status, and proliferation index, some of which are often associated with prognosis and response to therapy. However, further technical development is still needed to make CEST a reliable clinical application for body imaging and establish its role as a predictive and prognostic biomarker.

Graphical Abstract

Chemical Exchange Saturation Transfer (CEST) MRI, has gained recognition as a valuable addition to the molecular imaging and quantitative biomarkers arsenal. In this review, we discuss

the applications of CEST outside brain, specifically CEST-MRI for body oncologic imaging as well as challenges associated with the transition to clinic.

Keywords

CEST; APT; MRI; oncologic imaging; body imaging

Introduction

The expansion of available imaging techniques has impacted all aspects of cancer care, including screening, diagnosis, staging, monitoring of treatment response, and surveillance. Yet, despite numerous advances in oncologic imaging over the past several decades, there is still a need to provide more accurate diagnosis, offer better treatment guidance, and determine therapeutic success earlier[1,2]. Moreover, the development of increasingly targeted therapies demands imaging techniques that can provide objective, quantifiable information about the tumor micro-environment at the molecular, metabolic, and physiological levels. Compared to tissue-based analysis requiring one or multiple biopsies to characterize the entire disease burden, imaging has the potential to offer a non-invasive, spatially resolved whole-tumor evaluation of cancer biology in virtually any anatomic location of the body.

Magnetic Resonance Imaging (MRI) is an integral part of oncologic imaging, providing superb visualization of soft tissues without the use of ionizing radiation. MRI offers a range of quantitative image acquisitions (i.e., sequences) that are sensitive to molecular and pathophysiological information, such as Dynamic Contrast Enhanced (DCE) MRI, Magnetic Resonance Spectroscopy (MRS), Diffusion Weighted Imaging (DWI), Dynamic Susceptibility Contrast (DSC), and Arterial Spin Labeled (ASL) MRI. Multi-parametric MRI (mpMRI) approaches in which one or more of these quantitative sequences are added to standard anatomic sequences are gaining recognition as an important tool to provide tissue information beyond anatomic depiction of the tumor size and its boundaries[3–5]. However, despite these advances, further improvement is necessary for characterization of both localized and diffuse disease. Furthermore, some of these tools hold promise to play a larger role in treatment planning and imaging follow-up. For example, breast MRI using DCE offers the best reported sensitivity for diagnosis of breast cancer among the currently available imaging modalities[6–11]; however, its high cost and the need for administration of gadolinium-based contrast agents (GBCA) hampers wide adaptation. DWI does not require administration of GBCA and has been reported to offer slightly increased specificity compared to mammography[12]. Other methods such as Diffusion Tensor Imaging (DTI) are being explored[13]. Similarly, while MRI has revolutionized prostate cancer management in the last decade enabling targeted biopsies of MRI-visible suspicious lesions, its ability to accurately separate indolent from clinically significant cancers is limited[4]. Ideally, these non-invasive quantitative imaging techniques would provide objective information about tumor biology and aggressiveness (i.e., disease that forms, grows, or spreads quickly[14]), independent of tumor size or burden of disease. Furthermore, they would detect changes in the tumor microenvironment that occur prior to changes in tumor size so that therapy can be optimized early during treatment, as needed. Overall, these opportunities and

challenges point to the need to develop both non-invasive predictive and prognostic imaging biomarkers.

Recently, Chemical Exchange Saturation Transfer (CEST) MRI, has gained recognition as a valuable addition to the molecular imaging and quantitative biomarkers arsenal. Specifically, a sub-set of CEST, the Amide Proton Transfer weighted (APT or APTw) MRI that exploits saturation exchange from amide chemical groups, mostly at 3.5 ppm, was found useful in numerous applications for characterization and treatment of gliomas, such as differentiation and grading[15–17], characterization of the isocitrate dehydrogenase (IDH) mutation status[18,19], identifying 1p/19q codeletion status,[20,21] prediction of response to therapy [22,23], monitoring treatment response [24] and estimating overall prognosis[25]. An attractive characteristic of APT imaging is its sensitivity to tissue pH and protein concentration [26,27]. Indeed, APT is becoming commercially available in clinical MRI scanners[28]. While the majority of reported APT studies to date have focused on brain applications [29] such as malignancy [15–17,30,31] and stroke [26,32,33], CEST (and APT) has also shown promise in applications throughout the body.

The growth of interest in CEST technology can be emphasized with a literature search. Figure 1 illustrates the number of CEST publications over the last two decades. Since the introduction of the term "CEST" in early 2000 by Balaban et al. [34–36], the reported number of studies has continued to increase (>800 in total), with many focusing on the study of metabolism in cancer. Simultaneously, the number of reported studies translating these methods into clinical research involving human subjects has increased. While strides have been made for translating CEST/APTw into clinical neuro-oncology (exemplified by 361 total CEST publications involving neuroimaging), a similar translation to body oncology applications lags behind (143 CEST publications involving body imaging) (Figure 1, green vs. red). The slower migration of CEST-MRI to non-neurologic applications (recently also discussed by Gao et al.[37]) is likely a reflection of the technical challenges inherent to abdominal imaging. Specifically, the acquisition of CEST-MRI outside the brain is associated with salient features related to lipid artifacts, increased B_0 and B_1 inhomogeneity, and physiological motion (e.g., respiration, peristalsis, cardiac motion). In this review, we discuss the application of CEST-MRI to oncologic conditions of the breast and torso (i.e., body imaging) emphasizing the current applications reported in the literature. We discuss the above-mentioned challenges and their potential solutions. Specifically, we emphasize the technical barriers that prevent a wider adoption of CEST-MRI in body applications. Furthermore, we review the existing literature about the value of CEST-MRI in the context of other clinical state-of-the-art imaging techniques.

Examples of CEST-MRI for Body Imaging Applications

Breast Cancer

Breast cancer was one of the first reported applications of CEST outside brain and the musculoskeletal system, and it remains a major focus of development. Table 1 summarizes some of the reported technical characteristics employed in breast CEST-MRI.

Schmitt *et al.*[38] were one of the first to use CEST-MRI to characterize 6 breast cancers in 6 patients. The authors quantitatively assessed the lesions with the standard Magnetization Transfer Ratio asymmetry (MTR_{asym}) metric [26]. Three lesions displayed increased MTR_{asym} compared to normal-appearing fibroglandular tissue. The optimal chemical shift to observe the difference between healthy and malignant tissue was between 1.2 and 1.8 ppm. The authors speculated that increased concentration of choline and its derivatives was the cause for their findings. However, no differences were observed in the other three patients, which could be attributed to lipid artifacts. Indeed, one of the limitations of this study was presence of lipid signal (since no fat suppression was used), which is known to complicate the interpretation of the CEST acquisition data [39]. Nevertheless, this preliminary study illustrated the potential of CEST-MRI for evaluation of breast cancer.

Dula *et al.* [40] evaluated the feasibility of APT imaging at 3T for assessment of chemotherapy response. A CEST sequence was implemented, and its reproducibility was evaluated in 10 healthy controls. Furthermore, preliminary results were provided in three women with locally advanced breast cancer that demonstrated complete pathologic response, partial response, and progressive disease. An increase in APT values was observed in the patient with progressive disease (Figure 2, A). In contrast, a decrease in APT was observed in the two patients experiencing complete and partial response, respectively. In a different study conducted in healthy volunteers by the same group [41] focusing on the optimization of the acquisition protocol, special fat suppression methods were developed at 7T, based on water-only excitation via binomial pulses. Along with a dedicated RF coil, a short TE acquisition scheme and other optimizations, APT effects in non-neoplastic breast tissue were measured with a standard deviation of ~1%. These proposed protocol optimizations resulted in a four-fold reduction of the standard deviation compared to the previous 3T publication by the same group, illustrating that careful selection of acquisition parameters can lead to improved APT analytical performance. Both studies reported comparable APTw values of 4% and 5% at 7T and 3T, respectively. The same group reported further optimization of their 7T protocol [42] in healthy subjects focusing on 3.5 ppm (APT), and 1.5 ppm, which they proposed was associated with increased concentration of hydroxyl protons in glycosaminoglycans (GAG). A steady-state approach was employed, where a short saturation pulse is interleaved with a multi-shot acquisition, and the k-space is mapped out-in, leading to saturation build-up by the time the center of k-space is reached [43]. The reproducibility of their method was assessed using the intraclass correlation coefficient (ICC), which was 0.963% for APTw and 0.903% for the hydroxyl group. Furthermore, a single Lorentzian fit was used to identify the water position and this single Lorentzian fitted line was subtracted to calculate the CEST effects. This processing approach may allow better separation of the CEST effects from Nuclear Overhauser Effect (NOE), which appears at around −3.4 ppm and may contaminate the MTR_{asym} calculation.

Krikken *et al.* [44] used CEST-MRI at 7T to assess chemotherapy response in nine breast cancer patients with 10 tumors. CEST-MRI was performed before and after the first cycle of neoadjuvant chemotherapy. The CEST effect was estimated using a three-pool Lorentzian fit of the Z-spectra (water, APT, and magnetization transfer [MT]). Overall, the normalized mean APT for non-responders increased after therapy, while it was unchanged or decreased

for patients exhibiting partial or complete response (Figure 3, A). However, this response pattern was not universal with individual patients deviating from this behavior.

Zhang *et al.* [45] applied CEST-MRI at 3T to study the relationship between the CEST effect and histologic markers of aggressiveness (e.g., the estrogen receptor (ER) status and the cell proliferation index Ki-67) in 10 breast cancers in 10 patients prior to biopsy. A multi-point Dixon acquisition was used to separate fat and water signals before CEST postprocessing, and to collect a B_0 map for inhomogeneity correction (Figure 2, B). CEST was characterized at three frequency ranges: 1.0, 2.0, and 3.5 ppm, which were presumed to correlate to hydroxyls, amines, and amides concentration, respectively. A standard MTR_{asym} analysis was used. The cancers lacking expression of the estrogen receptor ([ER-]) demonstrated increased MTR_{asym} compared to ER+ cancers or benign tumors (Figure 3, B), with the largest differences observed in the 1.0 ppm and 2.0 ppm ranges. A linear positive correlation between MTR_{asym} and Ki-67 immunostaining in tissue was also observed, with the strongest correlation also in the 1.0 ppm and 2.0 ppm ranges. The observation of a positive correlation between the CEST effect and Ki-67 expression agrees to that previously reported in glioblastoma multiforme (GBM) [24]. However, the best differentiation of tumor grading and the strongest correlation with Ki-67 staining were found in the 3.5 ppm range in such report[24]. Overall, these studies indicate the potential role of CEST as a tool for non-invasive characterization of tissue biomarkers such as Ki-67 or the ER status.

Recognizing the important yet confounding role that fat plays in CEST-MRI, especially in the breast, Zimmermann *et al.*[46] proposed a special normalization procedure compensating for lipid-induced artifacts. Specifically, an apparent exchange-dependent relaxation (AREX) approach[47] that compensates for T_1 relaxation, corrects for B_1 inhomogeneity, and includes a five-pool Lorentzian fit method was utilized. Loi *et al.*[48] applied a similar protocol to investigate whether fat-corrected and relaxation-compensated APT and guanidyl (2.2 ppm) CEST can differentiate breast cancers from normal-appearing breast tissue in 10 cancer patients and 7 healthy volunteers (Figure 2, C). The study demonstrated increased APTw and guanidyl CEST in cancer lesions as compared to normal-appearing breast tissue (Figure 3, C). A positive correlation with Ki-67 was also observed, similar to the results reported by Zhang et al.[45]

Zaric *et al.* [49] investigated the correlation between CEST-MRI at 7T and both tumor grade and Ki-67 expression in 18 patients with primary breast cancer. MTR_{asym} was calculated at the maximum of the MTR_{asym} curve (Figure 2, D). A statistically significant difference in MTR_{asym} was observed between grade 1 (lower aggressiveness) and grade 3 (highest aggressiveness) cancers; however, statistically significant differences between grades 1 and 2, or between grades 2 and 3 cancers were not observed (Figure 3, D). Interestingly, the maximum values for MTR_{asym} were located at different positions of the Z-spectrum for different tumor grades. As with previous reports[45,48], there was a strong positive correlation between the CEST effect and Ki-67 staining.

Meng *et al.* [50] compared the diagnostic performance of diffusion kurtosis imaging (DKI) and APTw imaging in 133 patients with 135 breast lesions for the differentiation of benign breast lesions and cancers. The authors also evaluated a correlation between the MRI measures

and the histologic/molecular features of breast cancer (i.e., grade, ER/progesterone receptor [PR]/ human epidermal growth factor receptor 2 [Her-2], Ki-67). The CEST effect was estimated using the MTR_{asym} (3.5 ppm) metric. The mean MTR_{asym} was higher in benign lesions, contradicting previous studies in breast cancer [45,51], as well as APT studies in other cancer types [17,52,53]. However, high-grade cancers had a higher MTR_{asym} compared to low-grade cancers, which agrees with previous studies.

Zhang et al. [54] recently investigated APTw imaging for the early assessment of treatment response in 51 patients with triple-negative breast cancer (TNBC). CEST scanning was performed at baseline, and after two and four cycles of neoadjuvant therapy (three scans total). Two B_1-power levels (0.9 and 2.0 μT), as well as two analysis methods (MTR_{asym} and two-pool Lorentzian fit (0 and 3.5 ppm)) were evaluated to determine the most sensitive combination to detect therapy changes. Notably, the combination of 2.0 μT with MTR_{asym}, or the 0.9 μT with Lorentzian fit were most sensitive, indicating that the choice of saturation parameters may depend on the processing and analysis method, thus pointing to the need of standardization of these methodologies across the field. A statistically significant decrease in APTw signal was found after two therapy cycles in participants later exhibiting a pathologic complete response. However, APTw imaging was unable to differentiate patients exhibiting pathologic complete response from those who had partial response (i.e., residual disease after therapy).

A recent study by Liu et al.[55] evaluated the diagnostic performance of APTw imaging and its association with pathologic metrics of breast cancer. A statistically significant higher APTw was found in malignant tumors compared to benign lesions. Furthermore, the APTw effect increased with histologic grade and T-stage. However, there was only moderate correlation between APTw and Ki-67 expression in patients with IBC-NST (invasive breast carcinoma of no special type). An increase in APT was also observed in mucinous carcinoma (MC).

An interesting study by Loi et.al.[56] investigated the influence of the menstrual cycle on CEST in breast. Ten healthy premenopausal women were recruited. The study compared CEST (APT, as quantified by AREX) acquired during the first half (day 2–8) and the second half (day 15–21) of the menstrual cycle. No statistically significant differences were observed in the APT signal. DCE MR-mammography is known to be affected by water content changes in fibroglandular tissue during the menstrual cycle. Thus, the study is significant in indicating that observed APT changes in breast cancer are driven by malignant alterations and not by fluctuations due to menstrual cycle.

Finally, CEST was used in the evaluation of lymphedema related to breast cancer treatment. Donahue et al. [57] recruited and compared APTw imaging in seven patients with this complication versus healthy controls. CEST was estimated by MTR_{asym} as well as by subtraction from the Lorentzian baseline methods. An increased APTw signal in patients with lymphedema was observed compared to healthy controls. Moreover, APTw values increased with increasing lymphatic impairment. A subsequent study by Crescenzi et al. [58] estimated CEST-MRI changes at 3T in the upper extremities of 12 participants with lymphedema before and after standardized manual lymphatic drainage therapy. Notably, B_1 dispersion experiments were performed, where Z-spectra were acquired at a range of

B_1 values (1–3 μT, steps of 0.5 μT). The following quantitative CEST metrics were used and corrected for B_1 inhomogeneity: proton transfer ratio (PTR), MTR_{asym}, and AREX (all at 3.5ppm). A statistically significantly increase in PTR was reported following drainage therapy.

Overall, most studies have described an increase in CEST signal in cancers (compared to benign tissue) and suggest more pronounced CEST increases in more aggressive cancers (i.e., higher histological grade or Ki-67 proliferation index) compared to less aggressive cancers. The variations in APTw signal are largely attributed to changes in protein concentration. Similarly, changes in the 1 to 2 ppm range have been observed in breast cancer and could be potentially attributed to hydroxyl protons associated with choline derivatives, which are known to be increased in *in vitro* studies [59]. Additionally, an association between 1.5 ppm CEST effect and hydroxyl protons in GAG has been reported [42]. Notably, in lymphedema patients, the use of the well-described fluid-suppression CEST approach in the brain[60,61] may need to be applied, as to remove potential confounding factors of pooling extracellular fluid. Additional investigation on the origins of the CEST changes as well as an expert's consensus on acquisition and analysis methodologies will enable better interpretation of future studies.

Prostate Cancer

There is a limited number of reports about the use of CEST-MRI to characterize prostate cancer. Studies to date were conducted at 3T and used relatively short saturation (0.5 s), with high duty cycle and high B_1 intensity pulses (>2 μT). A summary of CEST-MRI acquisition parameters is provided in Table 2. A motivation for using CEST in prostate cancer is the fact that high-grade prostate cancer exhibits higher tumor cell proliferation rate and cellular density than clinically indolent prostate cancer. These histologic changes support the possibility that elevated mobile protein levels may exist in higher grade tumors and might be detectable by APTw imaging.

Jia *et al.* [62] evaluated the ability of APTw to differentiate prostate cancer in 12 biopsy-confirmed cancer patients scheduled for prostatectomy, with a median Gleason Score (GS) of 7 (range 7–9). Cancerous areas were compared with benign peripheral zone (PZ) areas. APTw images were co-registered with pathology images using anatomical markers on clinical T_2-weighted images (Figure 4, A) and APT was subsequently estimated using MTR_{asym} (3.5 ppm). A group analysis demonstrated that although the APTw difference between cancers and benign PZ was statistically significant, there was substantial overlap, limiting its clinical utility in individual cases. Furthermore, differentiation of cancers based on their histopathologic aggressiveness (i.e., Gleason score [GS]) was not possible. It should be noted that a relatively short CEST saturation was used in this study (496 msec), and no fat suppression was applied.

Takayama *et al.* [63] evaluated the association of APTw imaging with GS in prostate cancer at 3T MRI. Sixty-six prostate cancer patients, including 75 non-cancerous peripheral zone regions and 70 benign prostatic hyperplasia (BPH) nodules were included in the final analysis. The authors used alternating parallel transmission allowing for generation of 100% duty cycle saturation train for an extended period of time and an overall 0.5 sec

saturation length with 2 μT. All data were acquired under free breathing conditions and no post-processing for motion correction was performed. No fat suppression was applied. Patients were divided into four groups according to their GS (i.e., score of 6, 7, 8 and 9). Prostate cancer with GS-7(intermediate-risk cancer), showed the highest APTw signal intensity among the four groups, with this difference reaching statistical significance between GS7 and GS6 and between GS7 and GS9. However, the APT did not show a statistically significant correlation between non-cancerous peripheral zone regions and each of the prostate cancer groups, limiting its clinical utility. Potential confounding factors in this study include short saturation length, lack of correction for motion, non-suppressed fat signals, and the use of systematic 12-core needle biopsies as a reference standard, which is known to both miss clinically significance cancer and underestimate GS compared to MRI-targeted prostate biopsies [64].

A recent study by Yin *et al.* [65] assessed the diagnostic value of APTw and DKI in the evaluation of 49 patients with prostate cancer and 51 patients with BPH. APTw in prostate cancer was significantly higher than in BPH (Figure 4, B). APTw (quantified by MTR_{asym}(3.5 ppm)) showed moderate correlation with GS. One potential explanation to the different observations in this study *vs.* Takayama *et al.* [53] is that only larger (>300 mm^3) lesions were selected in the latter study, potentially harboring different histologic features (e.g., necrosis) that could affect the CEST data. At the same time, in the Yin *et al.* study, cancerous lesions with higher GS of 10 were included, which exhibited higher MTR_{asym} values contributing to improved correlation statistics.

Overall, the number of the studies evaluating the role of CEST in prostate cancer is limited. To date, no study has demonstrated a clear utility of CEST in the differentiation of prostate cancer from non-neoplastic prostate tissue or in the characterization of prostate cancer aggressiveness. However, further technical optimization of the CEST acquisition may improve these results.

Liver Disease

Chen *et al.* [66] evaluated the feasibility and reproducibility of liver CEST at 3T. The study enrolled eight healthy volunteers, without history of liver disease. A single slice TSE with fat suppression was used for acquisition during respiratory breath-hold. A relatively short, rectangular, RF saturation pulse of 0.3 sec and 3 μT intensity was used. The subjects were scanned multiple times over several days to assess the reproducibility of CEST imaging. The MTR_{asym}(3.5 ppm) was quantified as APTw value and the mean MTR_{asym} in the frequency range of 0.5 to 1.5 ppm was estimated as GlycoCEST. Liver APTw and GlycoCEST measurements had 95% limits of agreement of −0.842% to 0.899% and − 0.344% to 0.164%, respectively. The study demonstrated that CEST-MRI of the liver is feasible although further technical optimization of saturation scheme, acquisition, and post-processing are required to improve reproducibility.

Deng *et al.* [67] evaluated the effect of over-night fasting on CEST estimates in the liver with similar acquisition parameters to the previous study by Chen *et al* [66]. The study also evaluated the influence of different sets of Z-spectral offsets (41, 31, and 21 points) for the CEST calculation. The authors observed that both APTw and GlycoCEST decreased after

fasting, as expected due to the physiologically lower concentration of liver glycogen after fasting. It was also observed that decreasing the number of offsets led to more heterogeneous and noisier CEST maps. Their work indicates the potential of CEST to detect physiological changes in the liver.

A study by Tang *et al.* [68] used the organoiodine compound Ioversol and CEST-MRI to map extracellular pH (pH_e) in hepatic tumors. Ioversol is a widely used non-ionic X-ray contrast agent with high hydrophilicity and low toxicity. The CEST effect of this agent was quantified using MTR_{asym} at 4.3 ppm, which was associated previously with the pH-dependent CEST peak in the Ioversol Z-spectrum [69]. A so-called generalized ratiometric analysis was applied to derive pH_e. Briefly, the method *in vivo* uses a ratio of MTR_{asym} obtained using short RF pulses at two saturation power levels (B_1 of 0.2 and 1.15 μT) to derive pH_e. This approach was previously validated in animal models of breast and liver cancer [69]. Tang *et al.* [68] validated this methodology in phantoms and applied it to a cohort of 15 subjects diagnosed with hepatic carcinoma and five subjects with benign hepatic hemangioma. Subjects received 60 ml of Ioversol at 1 mL/sec injection rate. To reduce the washout effect for pH measurement, additional Ioversol was infused at 0.15 mL/sec for 5 min during CEST data acquisition. To reduce respiratory artifacts, the subjects were instructed to hold their breath, and an automated acquisition trigger was applied during the periods when they were holding their breath. Examples of pH_e maps of a carcinoma and a hemangioma are shown in Figure 5. The authors reported a statistically significant lower pH_e in hepatic carcinoma (6.66 ± 0.19) than that in hepatic hemangioma (7.34 ± 0.09). There was no difference between the pH values of hemangioma and normal liver tissue (7.34 ± 0.09 *vs.* 7.37 ± 0.08).

A recent study by Seo *et al.*[70] had evaluated the feasibility and accuracy of the APT imaging to characterize Focal Liver Lesions (FLL). Single slice TSE was used for imaging with saturation consisting of four RF pulses of 200 msec duration each and 1.0 μT. Multiple breath-holds were implemented for motion control. A B_0-map was collected using separate FFE sequence. A total of 203 patients were imaged using this APT protocol. The overall technical success rate was 62.1%, with the high failure rate attributed to large B_0 inhomogeneity, respiratory motion, or the combination of both. Among successful cases, MTR_{asym} values were significantly higher in metastases than those of hepatocellular carcinomas (0.13 ± 2.15% *vs.* − 1.41 ± 3.68%, p = 0.027). This study illustrates the challenges of CEST in the body applications. While APT for liver applications is promising, technical challenges remain a limitation for wide implementation.

Rectal Cancer

Nishie *et al.* [52] investigated the usefulness of APTw imaging to predict tumor grade in rectal cancer. Twenty-two patients underwent APTw MRI for evaluation of rectal cancer one month prior to surgery. An intramuscular injection of butylscopolamine (Buscopan 20 mg; Nippon Boehringer Ingelheim, Tokyo, Japan) was given to prevent image degradation due to bowel motion before the patient entered the MR scanner. The study was conducted at 3T and employed a saturation pulse of 0.5 sec and B_{1rms}=2 μT preceding a fat suppressed, single-slice single-shot fast spin-echo acquisition. Standard MTR_{asym} (3.5 ppm) was used to

quantify APTw. APTw values of tumors with a diameter of 5 cm or more (MTR_{asym} = 3.09 ± 1.41%; n=11) were significantly higher than those of tumors with a diameter of <5 cm (1.83 ± 1.38%; n=11). In addition, APTw of moderately differentiated adenocarcinoma (2.82 ± 1.51%) was significantly higher than that of well-differentiated adenocarcinoma (1.24 ± 0.57%) (Figure 6, A). There was no correlation of the APTw signal with Ki-67 staining.

In a follow up study, Nishie *et al.* [71] also investigated if APT could predict tumor response to neoadjuvant chemotherapy (NAC) in locally advanced rectal cancer (LARC). The study enrolled 17 subjects with LARC who underwent CEST-MRI and subsequently received at least two courses of NAC. MRI was conducted at 3T, and saturation and acquisition parameters were similar to their previous study. The mean APT of the low-response group (3.05 ± 1.61%; n=12) was significantly higher than that of the high-response group (1.14 ± 1.13%; n=5). Examples are shown in Figure 6, B. However, overlap between APTw values between the two groups was also observed.

While promising, the study had several limitations from a technical perspective, including lack of fat correction and relatively short saturation time (500 ms). Furthermore, the presence of air in the rectum may cause local B_0 inhomogeneity and substantial artifacts in CEST-MRI.

Li *et.al.*[72] compared APTw imaging and Diffusion Weighted imaging in assessment of pathological markers p53 and Ki-67 in rectal adenocarcinoma. The study had found that high-grade tumors (G3), more advanced stage tumors, and tumors with lymph node involvement had higher APT mean values, as quantified by MTR_{asym}(3.5 ppm). Moreover, tumors with p53-positive status had higher APT mean than tumors with negative p53 status (MTR_{asym}= 2.363 ± 0.457 vs. 2.0150 ± 0.3552, P = 0.014). In addition, APT was also statistically significant (P<0.001) different in tumors with low vs high Ki-67 status (MTR_{asym}= 1.7882 ± 0.11386 vs. 2.3975 ± 0.41586). The observed correlation with Ki-67 is analogous to the observations in breast[45] and brain tumors[17], but contradictory to the study by Nishie, *et.al.,* cited above[52]. The authors speculate that the difference in observations may stem from differences in tumor types, sample size, and the details of APT sequence implementation.

In a following study, the same group[73] had applied a 3D APT sequence to predict the pathologic factors for rectal adenocarcinoma. Consistently with other study of rectal adenocarcinoma, it was found that APT is significantly higher in high-grade (G3) vs low grade (G1 &G2) tumors; higher pT stage (T3 vs T3); as well as in tumors with lymph involvement (pN1–2 vs pN0).

Li *et.al.*[74] evaluated APTw imaging and intravoxel incoherent motion (IVIM) imaging as prognostic tools for rectal adenocarcinoma and compared them with DWI. The study was conducted at 3T and employed a saturation pulse of 2 sec and B_1=2 μT, followed by a fat-suppressed 3D TSE acquisition. Pathological reports were collected, including histological types, tumor grade, pathological stage, perineural invasion, lymphovascular invasion, cut edge infringement, and immunohistochemistry. Out of 110 cases scanned and analyzed, 17 cases were mucinous adenocarcinoma (MC) and 93 cases were rectal common

adenocarcinoma (AC). AC group was further differentiated by high-grade (G3) or low-grade (G1 and G2); by stage pT1–2 or pT3–4; and other pathological factors. It was observed that APT was significantly higher in MC than AC (P<0.001). It was hypothesized that MC is characterized by tumor cell hypersecretion and high mucus content, which may have contributed to the higher APT values. In addition, APT values in the low-grade tumors were significantly lower than in the high-grade (P=0.001). Other pathological grouping resulted in no statistically significant differences in APT.

Overall, these studies show that more aggressive tumors (i.e., defined by histologic tumor grade or other criteria, such as Ki-67 expression level and p53 mutation status) demonstrate increased APT, similar to brain, breast and prostate cancers.

Thorax

Ohno et al. [75] investigated the utility of APT for characterization of thoracic lesions. Twenty-one subjects were enrolled and scanned with CEST-MRI at 3T prior to surgery. Pathology examinations resulted in a diagnosis of 13 malignant and 8 benign thoracic lesions. Malignant lesions included 9 lung cancers (n=6 adenocarcinomas, n=3 squamous cell carcinomas) and 4 other thoracic malignancies. The saturation RF consisted of 0.4 sec pulse at B_{1rms}=1–2 µT (as limited by SAR). Cardiac- and respiratory-gated 2D fast spin-echo was used for acquisition. APTw was quantified using standard MTR_{asym} (3.5 ppm). The authors reported a number of statistically significant differences in MTR_{asym}(3.5 ppm), including: 1) higher values for malignant tumors (3.56 ± 3.01 %) than that for benign lesions (0.33% ± 0.38 %); 2) higher values in other thoracic malignancies (6.71 ± 3.46 %) than for lung cancer (2.16±1.41); and 3) higher values for adenocarcinoma (2.88±1.13%) than that for squamous cell carcinoma (0.71± 0.17%).

The results are promising, but the number of studies is very limited. It should be noted that lungs are particularly challenging area for CEST, due to factors such as increased B_0 inhomogeneity because of air presence and increased motion.

Uterus

Takayama et al. [53], evaluated APT for the assessment of histologic grades of endometrioid endometrial adenocarcinoma (EEA). The study, conducted at 3T, analyzed pre-surgical CEST-MRI of 32 patients with pathologically confirmed EEA, further classified into histologic grades: grade 1 (n = 11), grade 2 (n = 11), and grade 3 (n =10). Similar saturation, acquisition and post-processing scheme was used compared to other studies by the same group described above [52,71]. APT was positively correlated with the histologic grades of EEA, which is consistent with the results in other tumor types.

Luo et.al[76]., investigated application of Dynamic Glucose Enhancement (DGE[77–79]) CEST-MRI at 3T to non-invasively image glucose transport in the human placenta. CEST MRI is sensitive to glucose presence due to CEST effect from hydroxyl protons. DGE provides time resolved CEST signal due to the presence of exogenous glucose. In the study, the pregnant patients were given 50 gm of the glucose drink (Trutol™), which is comparable to the glucose tolerance test. CEST measurements were performed before the drink and DGE after. Five subjects were recruited. In all subjects, the increase in DGE signal was observed

within 30 min after the glucose drink. The study had demonstrated the feasibility of DGE in human placenta.[80,81]

Li *et.al*[80]. applied APTw imaging and Intravoxel Incoherent Motion (IVIM) for the diagnosis and differentiation of squamous cell carcinoma of the cervix (SCCC). The study, conducted at 3T, analyzed the data of 32 patients and 20 controls. It was found that the APT of SCCC (MTR_{asym}= 2.92 ± 0.24%) was higher than that of normal cervical stroma (MTR_{asym}= 2.72 ± 0.36%, P = 0.02). Moreover, a significant difference was found in the APT effect between the well-moderately differentiated SCCC group and the poorly differentiated SCCC group (P = 0.006). Same group.[82], investigated the utility of APTw imaging in estimating histologic grades of squamous cell carcinoma of the cervix (SCCC). It was found that APTw values have a high correlation with SCCC grade, with the significant difference in APTw observed between tumor grade 2 and grade 3.

Tumor Acidosis measurements (AcidoCEST)

Quantification of the CEST effect in terms of exchange rate (or pH) and concentration is challenging. To this end, Longo *et al.* had proposed using exogenous agents for CEST-based pH mapping [83]. Specifically, the two CEST signals (at 4.2 and 5.6 ppm) produced by two different amide protons of Iopamidol (Isovue™), which is an FDA-approved contrast agent for computed tomography studies They proposed a ratiometric method, which allows to rule out the concentration effects of the bolus contrast agent and accurately measure pH in the 5.5–7.4 range. The method was developed and applied in an acute kidney injury model in animals [84]. Jones *et. al.* [85] further optimized this approach in animals and translated it to humans, describing this method as AcidoCEST for the first time. This approach enables measurements of extracellular pH (pH_e) as well as concentration of the agent in tissue. In this first application to humans, AcidoCEST was tested in two subjects: one with high-grade breast invasive ductal carcinoma, and one with metastatic ovarian cancer. The former produced unreliable pH_e measurements, which was attributed to low uptake of the agent. AcidoCEST in the patient with metastatic ovarian cancer showed higher uptake of the agent in the ovarian tumors *vs.* breast cancer, allowing for pH_e measurements in the tumors and the kidney. Moreover, this approach has been recently used for pH_e measurements in liver [68], as discussed above (Figure 5).

While preliminary, these studies in animals and humans support the potential role of CEST-MRI as a non-invasive method to quantify pH_e.

CEST acquisition challenges and (potential) solutions

Presence of lipids in tissue

Pixels with a substantial fat fraction (FF) display complex behavior in the CEST experiment, due to partial volume effects. A recent publication by Zhang *et al.* [39] demonstrated that such behavior is non-intuitive and is largely governed by the FF and echo time (TE). If not considered these variables lead to spurious CEST effects and complicated Z-spectra (Figure 7, A) that cannot be used reliably even with the most sophisticated post-processing available. This problem, although acknowledged [86], is not a particularly relevant issue in

brain CEST-MRI. However, it is a dominant factor for body CEST applications, since fat surrounds all the viscera and, in many tissues (*e.g.,* breast, pancreas), water and fat are spatially interleaved on the scale of the MRI spatial resolution, leading to partial volume effects. Moreover, presence of fat poses additional challenges for B_0 corrections.

The choice of TE influences the Z-spectra. Using in-phase condition or very short TE, might partially alleviate the problem, but the most effective solution would be a complete removal of the fat signals.

Methods relying on selective fat nulling (e.g., SPIR, binomial pulses, *etc.*, see Table 1) have been used for CEST applications in the body. However, such applications are associated with several challenges. First, the increased B_0 inhomogeneity makes selective pulse application challenging, thus degrading fat suppression. While a remaining fat signal of a few percent may be acceptable for anatomical imaging applications, CEST quantification is strongly affected even by small imperfections in fat suppression. Second, the introduction of RF fat-saturation pulses is typically done after CEST saturation and prior to the image acquisition. This inevitably introduces recovery of the saturated signal and decreases CEST contrast. In addition, the CEST saturation, if applied to fat frequencies during Z-spectral acquisition, may compromise the effect of fat suppression for inversion-based pulses like SPIR, as the inversion does not act on a pre-saturated fat signal. Third, any additional RF pulses result in an undesirable increase in SAR, leading to increased tissue heating and long scan durations (i.e., due to need to increase TR values to alleviate the SAR increase).

Efficient solutions would involve methods that bypass these limitations and rely on the distinct spectroscopic and phase properties of the water and fat signals. An example is the combination of CEST-saturation RF with multi-point Dixon [87] (mDixon or IDEAL [88–90]) acquisition (Figure 7, A), first introduced by Zhang *et al.* [45]. Here, at least 3 echoes are collected and used for the reconstruction of water, fat, and B_0. Ideally, the single-shot multi-point Dixon technique can be used [91], which requires acquisition of multiple echoes for the same k-space line, without increasing the total acquisition time notably.

Multi-point Dixon post-processing is available across all vendors and typically assumes a multi-peak fat spectrum [92]. However, CEST saturation (when applied at frequencies coinciding with the fat spectral peaks) alters the fat spectrum, which may lead to artifacts in mDixon reconstruction. Zhao *et al.* [93] proposed a self-adapting algorithm capable of accounting for the saturation influence and removing residual artifacts leading to a more accurate Z-spectra and CEST estimation (Figure 7, B).

An interesting approach was recently introduced by Zimmermann, *et al.* [46] based on the observation that the fat signal can be estimated by the residual signal at the spectral position of the direct water saturation. A normalization factor is introduced, which takes fat contribution into account. An example of this application is shown in Figure 7, C. The advantage of this method is that it solely relies on the data already acquired (in complex form), without the need for acquisition modifications or acquisition of additional echoes. A potential caveat is that the fat signal is calculated based on the direct water saturation, which itself may also be influenced by intravoxel dispersion [94].

B_0 and B_1 inhomogeneity

Accurate magnetic field inhomogeneity (B_0) correction is necessary for CEST since it relies on the precise identification of the applied off-resonance frequency. However, B_0 mapping methods, established in the context of CEST in the brain, do not always work well in the presence of a high fat fractions. One of the first proposed methods, and perhaps the simplest to use, relies on finding the minimum of the Z-spectrum and re-assigning the zero frequency to it. Typically, the acquired points are interpolated to a higher spectral resolution. The method is dependent on the number of points acquired around zero (deteriorating in accuracy with decreased number of points). It also assumes symmetric Z-spectra which may not be true due to inherent MT asymmetry [95]. This approach fails when the Z-spectrum is broad (due to MT) or when large FF is present. Furthermore, since the points acquired near to full water saturation have inherent low signal to noise ratio (SNR) and do not contain information about the off-resonant CEST pools, this correction method is inefficient and might not suitable for 3D organ coverage, which is more desirable for clinical applications. Nevertheless, implementation of this method is straightforward, does not require additional acquisitions beyond the Z-spectrum, and performs relatively well within its limits, which explains its popularity [49,58,96].

Another commonly used B_0 mapping technique (widely used beyond CEST) measures phase differences between two TE values[97]. However, true chemical shift difference from water (as observed in fat at −3.4ppm) might be erroneously considered as field inhomogeneity (a fat voxel will appear as a −3.4 ppm field shift). Thus, this method fails in fat-containing voxels. Hence, its utility in body CEST-MRI is limited. Dixon-based B_0 mapping techniques, as available on most clinical MRI systems, take the fat signal into account and can be used as alternative for separate B_0 mapping.

Water Saturation Shift Referencing (WASSR) is another widely used method [98], which employs a Z-spectrum acquired at low-power RF at the frequency range close to water, and searches for the minimum of this low-power Z-spectrum. This method has been used extensively in brain CEST-MRI studies [44,54]. While it is considered fairly accurate in those settings, the need for longer acquisition time (due to acquisition of an additional Z-spectrum) and its sensitivity to the presence of large FF also limits its utility in body applications.

The combination of CEST with Dixon reconstruction described above bypasses the limitations imposed by large FF for B_0 maps. Moreover, it offers an advantage of *concurrent* acquisition of B_0 maps, eliminating uncertainties associated with acquiring separate scans for B_0 mapping and CEST, such as interscan motion and hardware re-calibrations. Concurrent B_0 mapping also allows to correct for Eddy-current induced B_0 shifts, which result from the gradient switching applied during the CEST acquisition. At the same time, the approach might depend on the accuracy of the reconstruction, influence of saturation on the fat spectrum as well as the choice of echoes and echo times.

Another approach to map B_0 and B_1, simultaneously was introduced by Schuenke *et al.* [99]. Their Simultaneous Mapping of Water Shift and B1 (WASABI) method is based on Rabi oscillations due to off-resonance irradiation. It employs a preparation block and sampling

of several frequency offsets allowing the calculation of the absolute water frequency and B_1 amplitude. WASABI had been used at high field strength in several studies, including a study in breast cancer [46].

If the B_1 map is known (using WASABI or other B_1 mapping method) it could be used to correct CEST effect, as was proposed by Windschuh *et al.* [100] and Sun *et al.* [101]. However, a potential challenge is that CEST effect is non-linearly altered with B_1 and depends strongly on tissue properties. A CEST acquisition at multiple different B_1 levels is required for the B_1 correction. Moreover, since the presence or absence of CEST is unknown *a priori* such correction may not work if the saturation was not efficient or the CEST effect is low due to low concentration. Thus, currently available B_1 correction methods are not accurate or time efficient. To the best of our knowledge, so far, none of these B_1 correction methods had been reported outside of the brain. RF shimming combined with reduced FOV strategies to reduce B_1 homogeneity and associated errors in CEST may represent a more efficient approach.

Physiological Motion

Another challenge for CEST acquisitions in the body is the presence of physiological motion (e.g., respiratory, cardiac, peristalsis). First, motion leads to artifacts in the CEST maps. Respiratory-triggered acquisitions may improve the robustness of CEST acquisitions. However, the long RF saturation pulse (~1–5 s) needed in CEST acquisitions poses a problem for triggered acquisitions. In healthy subjects, the end-expiratory state is not only the longest time interval (i.e., about 1 s), but it is also the phase with the least motion. With standard triggering techniques commonly used in clinical practice, the pulse sequence starts at or shortly after the beginning of this favorable end-expiration time window. However, the need to apply a long RF saturation in CEST experiments leads to the acquisition readout starting outside/after the end-expiratory time window, inevitably leading to motion artifacts. Alternatively, if the RF saturation is performed during the inspiratory phase, the image acquisition can occur during the end-expiration. However, such approach requires specialized respiratory trigger mechanisms. Alternatively, the motion can be addressed via guided breathing, an approach similar to what has been reported for ASL acquisitions [102].

However, even with guided breathing techniques, motion might still compromise CEST acquisitions. Although post-acquisition registration methods can be applied, these are not straightforward because registration algorithms often rely on features associated with image contrast, which changes during off-resonance saturation, limiting some of the common registration methods. Welch *et al.* [103] introduced a solution bypassing this constraint, which employs a low-rank approximation of the Z-spectrum. This method was tested in phantoms and in human thigh during Creatine CEST acquisitions. An additional challenge is that abdominal organs move in multiple directions during respiration (i.e., not addressable even with non-rigid elastic registration algorithms). While other motion correction methods are under investigation, to the best of our knowledge they have not been reported for human CEST studies.

CEST *vs.* other imaging methods

A direct comparison of CEST-MRI with other imaging methods is generally lacking or has been reported in small cohorts, with a few exceptions. Here, we provide an overview of these studies.

Several studies compared CEST with DCE MRI[38] or diffusion-based methods[49,50,52,63,74,80]. Note that these MRI methods rely on inherently different contrast mechanisms. DCE relies on relaxation changes induced by an exogenous contrast agent taken up by tissue compartments; DWI (and DTI, DKI or IVIM) relies on differences in the diffusion of water molecules in tissue and it is influenced by tissue cellularity; and CEST image contrast results from a proton chemical exchange. Thus, the diagnostic performance of these techniques is expected to be different. While some of these methods may be preferred for specific clinical applications, they can play a complimentary role within a multi-parametric MRI examination.

Schmitt *et al.*[38] described that in 3 out of 6 breast cancer patients, there was a good agreement between CEST and DCE. However, CEST failed to identify tumors in three other patients. The lack of fat suppression in their acquisition may have limited the diagnostic performance of CEST-MRI.

Zaric *et al.*[49] collected DCE, DWI and CEST data at 7T in a cohort of 18 breast cancer patients. The maximum MTR_{asym} demonstrated high positive correlation with the proliferation index Ki-67. At the same time DWI-derived apparent diffusion coefficient (ADC) values demonstrated moderate negative correlation with Ki-67. The authors confirmed a moderate correlation between these two methods, which might be explained by differences in the processes contributing to CEST and DWI image contrast.

Meng *et al.*[50], compared the diagnostic performance of quantitative metrics derived from DKI (i.e., apparent kurtosis coefficient [K_{app}] and non-Gaussian diffusion coefficient [D_{app}]) and APTw (MTR_{asym}). K_{app} was moderately correlated with the pathological grade ($|r| = 0.724$) and mildly correlated with Ki-67 and HER-2 expression ($|r| = 0.454, 0.333$) in cancerous lesions. Similarly, D_{app} was moderately correlated with the pathological grade ($|r| = 0.648$) and mildly correlated with Ki-67 expression ($|r| = 0.400$) in cancerous lesions. In contrast, MTR_{asym}(3.5 ppm) was only mildly correlated with the pathological grade ($|r| = 0.468$) in cancerous lesions. Thus, the authors concluded that DKI was superior to APTw in the characterization of breast cancer. Importantly, their APTw results were contradictory to other studies, with a decreased MTR_{asym}(3.5 ppm) observed in cancerous lesions compared to benign lesions.

Takayama *et al.*[63] correlated APT and ADC to the Gleason Score (GS) in a cohort of 66 prostate cancer patients at 3T. ADC values showed a significant negative correlation with GS ($p<0.05$), while APT did not. At the same time, a recent study by Yin *et al.*,[65] also examined APT and DKI in prostate cancer and observed a moderate correlation between APT and GS ($r=0.640$, $p<0.05$), while mean kurtosis (MK) and mean diffusion (MD) were strongly correlated with GS ($r=0.844$ and 0.811, respectively, $p<0.05$). All three metrics

(MK, MD, and APT), were statistically different (p<0.05) between intermediate-risk, and high-risk groups and between prostate cancer and BPH.

Nishie *et al.* [52] compared APT and DWI in in the characterization of rectal cancer. The APT values were statistically different in larger (>5cm) tumors compared to smaller tumors (p=0.047). Similarly APT values were statistically different in moderately differentiated adenocarcinoma *vs.* well-differentiated adenocarcinoma (p=0.035). However, DWI-derived ADC values were not different between these groups.

Another study of rectal cancer, by Li L. *et al.*[72], had compared APT and DWI in assessing pathological factors as well as p53 and Ki-67 status in rectal adenocarcinomas. The study had observed that groups with positive p53 and high Ki-67 index exhibited higher APT compared to negative p53 and low Ki-67. At the same time, it was found that the tumors with high Ki-67 index showed lower ADC values (negative correlation). The was no difference in ADC values between positive and negative p53 groups. The ROC analysis had demonstrated that mean APT had the diagnostic ability in predicting p53 and Ki-67 status, while mean ADC demonstrated only weak ability in predicting Ki-67. It was concluded that overall APT might offer superior diagnostic performance than DKI, albeit the difference was not statistically significant.

Li J. *et al.*[74] compared APTw and IVIM imaging with DWI imaging for evaluation of prognostic factors in rectal carcinomas. APT, D and ADC were significantly higher in AC vs MC (P<0.001). In the AC group, APT and D values showed significant differences between low- and high-grade tumors (MTR_{asym} = 2.226 ± 0.347% vs. 2.668 ± 0.638%, and D=0.842 ± 0.148×10^{-3} mm^2/sec vs. 0.777 ± 0.178×10^{-3} mm^2/sec, respectively, both P<0.05). In addition, the D value had significant difference between positive and negative extramural vascular invasion (EMVI) tumors (D = 0.771 ± 0.175×10^{-3} mm^2/sec vs. D=0.858 ± 0.151×10^{-3} mm^2/sec, P<0.05). It was concluded that APT and IVIM were helpful to assess the prognostic factors related to rectal adenocarcinoma, including histopathological type, tumor grade and the EMVI status.

In the study mentioned earlier, Takayama *et al.* [53], evaluated DWI in addition to APT for the assessment of histologic grades of Endometrioid Endometrial Adenocarcinoma EEA. While APT exhibited a positive correlation with tumor grade (r=0.55, P = 0.001), no such correlation was observed for ADC metrics.

Overall, these studies suggest that CEST-derived metrics may outperform diffusion-based approaches in certain scenarios, which are influenced by lesion location and cancer type.

Li B. *et al.*[80] compared APTw imaging and IVIM in cervical cancer (SCCC, described above). The study indicated that APT may show a better performance than IVIM-derived parameters in predicting SCCC differentiation. The same group[82] compared APTw imaging with F^{18} FDG PET to predict histologic grades of SCCC (also described above). The authors observed that the maximum (SUV_{max}) and mean (SUV_{mean}) standardized uptake value in PET imaging were not significantly different between different tumor grades. At the same time, they observed high correlation of APT with SCCC grade. This might indicate that APT

is more accurate for SCCC pathological grading. To the best of our knowledge, it is a first report of a study comparing FDG PET and CEST-MRI outside brain.

Gaps and unmet clinical needs

MRI has revolutionized many aspects of cancer management, from detection to assessment and follow-up. However, new opportunities to address unmet clinical needs with novel MRI methodologies continue to arise as new therapies and our understanding of cancer evolves. Thus, CEST has the potential to play an increasingly crucial role, closing gaps in all the stages of diagnosis, prognosis and prediction of response to treatment[2].

This role will stem from the inherent sensitivity to metabolic and molecular processes, which is a differentiating feature of CEST compared to other available MRI technologies. While spectroscopy possess similar features, it is limited by prolonged acquisition times and the size of anatomic evaluation (i.e., small sampling region) compared to CEST. The ability of interrogating entire tumors with CEST provides an opportunity to explore molecular alterations, tumor microenvironment, and heterogeneity non-invasively, perhaps as a complementary tool to the small tissue samples obtained through tumor biopsies, for better tumor characterization.

For example, CEST-MRI could assist in the assessment and follow-up of breast cancer. Addition of CEST to state-of-the-art MRI protocols may help increase MRI specificity without reducing sensitivity when a breast MRI is requested to evaluate extent of disease for a known malignancy. Similarly, CEST-MRI could also potentially assist with more accurate evaluation or re-evaluation of patients undergoing neoadjuvant therapy, allowing early distinction of patients who respond from those who do not respond to therapy[1].

In its initial implementation, CEST may be added to mpMRI protocols to evaluate its performance in a variety of clinical scenarios. For example, data suggest that the addition of CEST to mpMRI protocols in patients with prostate cancer may help in the differentiation between those with clinically insignificant and significant prostate cancers[4].

The studies reviewed herein provide preliminary evidence that CEST-MRI may help address important unmet clinical needs through the exploration of tumor metabolic information. However, for CEST-MRI to fulfil its potential and become fully accepted in clinical practice, larger clinical studies proving its reliability, utility and superiority to other existing MRI methods are needed[3].

Future Directions

In the recent years, CEST-MRI studies focusing on body applications outside brain had demonstrated the feasibility and potential of this technique. However, larger studies are needed to validate this technique as a reliable and reproducible biomarker of disease status. To date, the most developed application outside brain is breast imaging although the number of patients reported remains low (Table 1).

Technical challenges reviewed here such as B_0 correction, lipid artifacts and physiological motion limit the broad applicability of this technique. However, technical challenges are often encountered when novel MRI methods are in early stages of development, particularly for quantitative techniques (e.g., ASL, DWI). The previous successes translating such quantitative MRI acquisitions to the clinic through systematic technical development and improvements is encouraging. Indeed, some of the technical advances described in this review such as improved fat removal and B_0 correction move the CEST MRI methods closer to routine clinical use. Further technical improvements in CEST-MRI should enable replacing the commonly used single-slice acquisition for multi-slice or volumetric acquisitions, as larger anatomic coverage is needed for virtually all applications in the body. However, the acquisition time is a competing factor since obtaining multiple images for Z-spectra is time consuming. For example, a CEST-MRI acquisition with three-dimensional (3D) anatomic coverage in reality represents a four- dimensional (4D) acquisition when taking the spectral Z-dimension into account. Longer acquisitions impede breath-hold imaging (i.e., free of breathing artifacts) and therefore require motion synchronization or/and correction. Moreover, long acquisition times may be incompatible with comprehensive multiparametric MRI examinations. Recently introduced acceleration methods employing compressed sensing[104–106] and deep learning[107] might enable larger anatomic coverage for CEST-MRI acquisitions within acceptable acquisition times.

Demonstrating robustness and reproducibility of CEST will be crucial to enable its routine use in the clinic. Dula et al.[42] used the intraclass correlation coefficient (ICC) to characterize the test-retest reproducibility of CEST-MRI reporting values greater than 0.9 (with 1 maximum possible), indicating strong agreement.

Another challenge arises from the different saturation schemes, acquisition parameters, and post-processing, implemented by the different MRI manufacturers and research groups in CEST research, which makes a direct comparison of results difficult. Recently, a unified library of RF saturation pulses was created to serve as a standard library for different vendors and research sites working on CEST development [108]. Another important step would be development of a standard CEST phantom, with the corresponding library of CEST effects and detailed record of experimental conditions under which it was measured[109]. Similarly, there is substantial variation in post-processing methods. For example, some novel methods employ solutions such as multi-pool fitting and correction for relaxation, making difficult to compare results with those of more basic MTR asymmetry analyses. As the field matures, a more unified approach will emerge.

Conclusion

There is increasing interest in the use of CEST-MRI for applications outside brain, particularly in oncology. Although preliminary, data suggest that there is a positive relationship between CEST and markers of aggressive histology such as higher tumor grade, receptor status, and high proliferation index. Some of these markers are frequently associated with resistance to therapy and worse prognosis. Therefore, there is hope that CEST may play an important role in management of oncologic patients. While an ideal application outside neuroimaging has not been identified yet, its application in breast cancer

patients is most mature. The routine clinical use of MRI for breast cancer detection, staging and monitoring of treatment response, as well as the recent developments in the characterization of breast cancer with CEST are indeed encouraging. However, further technical development is still needed to overcome challenges associated with imaging outside brain, such as the presence of lipids, physiologic motion, and increased B_0 inhomogeneity. Such developments are underway and should enable more robust application of CEST to a number of body oncologic conditions.

Acknowledgement

Abbreviations List

B_0	Magnetic Field Inhomogeneity
AC	Common Adenocarcinoma
ADC	Apparent Diffusion Coefficient
APT	Amide Proton Transfer
APTw	Amide Proton Transfer weighted
AREX	Apparent Exchange-Dependent Relaxation
ASL	Arterial Spin Labeled
BPH	Benign Prostatic Hyperplasia
CHESS	Chemical Shift Selective
CEST	Chemical Exchange Saturation Transfer
D	Diffusion Coefficient
DCE	Dynamic Contrast Enhanced
DSC	Dynamic Susceptibility Contrast
DKI	Diffusion Kurtosis Imaging
DTI	Diffusion Tensor Imaging
DWI	Diffusion Weighted Imaging
EEA	Endometrioid Endometrial Adenocarcinoma
EMVI	Extramural Vascular Invasion
ER	Estrogen Receptor

FF	Fat Fraction
FFE	Fast Field Echo
FLL	Focal Liver Lesions
FOV	Field of View
GAG	Glycosaminoglycan
GBCA	Gadolinium Based Contrast Agents
GBM	Glioblastoma Multiforme
GS	Gleason Score
Her-2	Human Epidermal Growth Factor Receptor 2
IBC-NST	Invasive Breast Carcinoma of No Special Type
IDC	Invasive Ductal Carcinoma
IDEAL	Iterative Decomposition of water and fat with Echo Asymmetry and Least-squares estimation
ICC	Intraclass Correlation Coefficient
IVIM	Intravoxel Incoherent Motion
LARC	Locally Advanced Rectal Cancer
MC	Mucinous Adenocarcinoma
MD	Mean Diffusion
mDixon	Multi-point Dixon acquisition and reconstruction
MK	Mean Kurtosis
mpMRI	Multi-parametric MRI
MRI	Magnetic Resonance Imaging
MRS	Magnetic Resonance Spectroscopy
MT	Magnetization Transfer
MTR_{asym}	Magnetization Transfer Ratio asymmetry
NAC	Neoadjuvant Chemotherapy
NOE	Nuclear Overhauser Effect
pH_e	Extracellular pH
PR	Progesterone Receptor

PTR	Proton Transfer Ratio
SAR	Specific Absorption Rate
SCCC	Squamous Cell Carcinoma of the Cervix (SCCC)
SS	Single Shot
SPIR	Spectral Presaturation with Inversion Recovery
T	Tesla
TE	Echo Time
TFE	Turbo Field Echo
TNBC	Triple Negative Breast Cancer
TR	Repetition Time
TSE	Turbo Spin Echo
WASABI	Simultaneous Mapping of Water Shift and B_1
WASSR	Water Saturation Shift Referencing

References

1. Hylton NM. Residual Disease after Neoadjuvant Therapy for Breast Cancer: Can MRI Help? Radiology. 2018/11/01 2018;289(2):335–336. doi:10.1148/radiol.2018181846 [PubMed: 30152746]

2. Nicolini A. Biomarkers: a framework driving advances in oncology. Biomarkers in Medicine. 2015/03/01 2015;9(4):303–306. doi:10.2217/bmm.15.7 [PubMed: 25808434]

3. Mendichovszky I, Pullens P, Dekkers I, et al. Technical recommendations for clinical translation of renal MRI: a consensus project of the Cooperation in Science and Technology Action PARENCHIMA. (1352–8661 (Electronic))

4. Stabile A, Giganti F, Rosenkrantz AB, et al. Multiparametric MRI for prostate cancer diagnosis: current status and future directions. Nature Reviews Urology. 2020/01/01 2020;17(1):41–61. doi:10.1038/s41585-019-0212-4 [PubMed: 31316185]

5. Hagiwara A, Tatekawa H, Yao J, et al. Visualization of tumor heterogeneity and prediction of isocitrate dehydrogenase mutation status for human gliomas using multiparametric physiologic and metabolic MRI. Article. Scientific Reports. 2022;12(1)1078. doi:10.1038/s41598-022-05077-2 [PubMed: 35058510]

6. Morrow M, Waters J, Morris E. MRI for breast cancer screening, diagnosis, and treatment. Lancet. Nov 19 2011;378(9805):1804–11. doi:10.1016/S0140-6736(11)61350-0 [PubMed: 22098853]

7. Mahoney MC, Gatsonis C, Hanna L, DeMartini WB, Lehman C. Positive predictive value of BI-RADS MR imaging. Radiology. Jul 2012;264(1):51–8. doi:10.1148/radiol.12110619 [PubMed: 22589320]

8. Pediconi F, Miglio E, Telesca M, et al. Effect of preoperative breast magnetic resonance imaging on surgical decision making and cancer recurrence rates. Invest Radiol. Feb 2012;47(2):128–35. doi:10.1097/RLI.0b013e318230061c [PubMed: 21934515]

9. Kuhl C, Weigel S, Schrading S, et al. Prospective multicenter cohort study to refine management recommendations for women at elevated familial risk of breast cancer: the EVA trial. J Clin Oncol. Mar 20 2010;28(9):1450–7. doi:10.1200/jco.2009.23.0839 [PubMed: 20177029]

10. Comstock CE, Gatsonis C, Newstead GM, et al. Comparison of Abbreviated Breast MRI vs Digital Breast Tomosynthesis for Breast Cancer Detection Among Women With Dense

Breasts Undergoing Screening. JAMA. Feb 25 2020;323(8):746–756. doi:10.1001/jama.2020.0572 [PubMed: 32096852]

11. Gordon PB. The Impact of Dense Breasts on the Stage of Breast Cancer at Diagnosis: A Review and Options for Supplemental Screening. Current Oncology. 2022;29(5):3595–3636. [PubMed: 35621681]

12. Amornsiripanitch N, Bickelhaupt S, Shin HJ, et al. Diffusion-weighted MRI for Unenhanced Breast Cancer Screening. Radiology. Dec 2019;293(3):504–520. doi:10.1148/radiol.2019182789 [PubMed: 31592734]

13. Luo J, Hippe DS, Rahbar H, Parsian S, Rendi MH, Partridge SC. Diffusion tensor imaging for characterizing tumor microstructure and improving diagnostic performance on breast MRI: a prospective observational study. Breast Cancer Res. 2019/09/04 2019;21(1):102. doi:10.1186/s13058-019-1183-3 [PubMed: 31484577]

14. https://www.cancer.gov/publications/dictionaries/cancer-terms/def/aggressive

15. Zhou J, Tryggestad E, Wen Z, et al. Differentiation between Glioma and Radiation Necrosis using Molecular Magnetic Resonance Imaging of Endogenous Proteins and Peptides. Nat Med. 2011;17:130–134. [PubMed: 21170048]

16. Zhou J, Blakeley JO, Hua J, et al. Practical data acquisition method for human brain tumor amide proton transfer (APT) imaging. Magn Reson Med. Oct 2008;60(4):842–9. doi:10.1002/mrm.21712 [PubMed: 18816868]

17. Togao O, Yoshiura T, Keupp J, et al. Amide proton transfer imaging of adult diffuse gliomas: correlation with histopathological grades. Neuro Oncol. Mar 2014;16(3):441–8. doi:10.1093/neuonc/not158 [PubMed: 24305718]

18. Jiang S, Zou T, Eberhart CG, et al. Predicting IDH mutation status in grade II gliomas using amide proton transfer-weighted (APTw) MRI. Magn Reson Med. Sep 2017;78(3):1100–1109. doi:10.1002/mrm.26820 [PubMed: 28714279]

19. Paech D, Windschuh J, Oberhollenzer J, et al. Assessing the predictability of IDH mutation and MGMT methylation status in glioma patients using relaxation-compensated multipool CEST MRI at 7.0 T. Neuro Oncol. Nov 12 2018;20(12):1661–1671. doi:10.1093/neuonc/noy073 [PubMed: 29733378]

20. Yao J, Hagiwara A, Raymond C, et al. Human IDH mutant 1p/19q co-deleted gliomas have low tumor acidity as evidenced by molecular MRI and PET: a retrospective study. Sci Rep. Jul 17 2020;10(1):11922. doi:10.1038/s41598-020-68733-5 [PubMed: 32681084]

21. Su C, Xu S, Lin D, et al. Multi-parametric Z-spectral MRI may have a good performance for glioma stratification in clinical patients. Eur Radiol. Jan 2022;32(1):101–111. doi:10.1007/s00330-021-08175-3 [PubMed: 34272981]

22. Mehrabian H, Myrehaug S, Soliman H, Sahgal A, Stanisz GJ. Evaluation of Glioblastoma Response to Therapy With Chemical Exchange Saturation Transfer. Int J Radiat Oncol Biol Phys. Jul 1 2018;101(3):713–723. doi:10.1016/j.ijrobp.2018.03.057 [PubMed: 29893279]

23. Regnery S, Adeberg S, Dreher C, et al. Chemical exchange saturation transfer MRI serves as predictor of early progression in glioblastoma patients. Oncotarget. 2018;9(47)

24. Sagiyama K, Mashimo T, Togao O, et al. In vivo chemical exchange saturation transfer imaging allows early detection of a therapeutic response in glioblastoma. Proc Natl Acad Sci U S A. Mar 25 2014;111(12):4542–7. doi:10.1073/pnas.1323855111 [PubMed: 24616497]

25. Paech D, Dreher C, Regnery S, et al. Relaxation-compensated amide proton transfer (APT) MRI signal intensity is associated with survival and progression in high-grade glioma patients. Eur Radiol. 2019/09/01 2019;29(9):4957–4967. doi:10.1007/s00330-019-06066-2 [PubMed: 30809720]

26. Zhou J, Payen J-F, Wilson DA, Traystman RJ, van Zijl PCM. Using the amide proton signals of intracellular propteins and peptides to detect pH effects in MRI. Nat Med. 2003;9:1085–1090. [PubMed: 12872167]

27. Ray KJ, Simard MA, Larkin JR, et al. Tumor pH and Protein Concentration Contribute to the Signal of Amide Proton Transfer Magnetic Resonance Imaging. Cancer Res. 2019;79(7):1343–1352. doi:10.1158/0008-5472.CAN-18-2168 [PubMed: 30679178]

28. Amide Proton Transfer weighted imaging: Advancement in molecular tumor diagnosis. 2018. http://images.philips.com/is/content/PhilipsConsumer/Campaigns/HC20140401_DG/HC-Master-White_paper_3D_APT_14062018.PDF

29. Zhou J, Heo HY, Knutsson L, van Zijl PCM, Jiang S. APT-weighted MRI: Techniques, current neuro applications, and challenging issues. J Magn Reson Imaging. Aug 2019;50(2):347–364. doi:10.1002/jmri.26645 [PubMed: 30663162]

30. Zhou J, Lal B, Wilson DA, Laterra J, van Zijl PC. Amide proton transfer (APT) contrast for imaging of brain tumors. Magn Reson Med. Dec 2003;50(6):1120–6. doi:10.1002/mrm.10651 [PubMed: 14648559]

31. Sotirios B, Demetriou E, Topriceanu CC, Zakrzewska Z. The role of APT imaging in gliomas grading: A systematic review and meta-analysis. Eur J Radiol. 2020/12/01/ 2020;133:109353. doi:10.1016/j.ejrad.2020.109353 [PubMed: 33120241]

32. Tee YK, Harston GW, Blockley N, et al. Comparing different analysis methods for quantifying the MRI amide proton transfer (APT) effect in hyperacute stroke patients. NMR Biomed. Sep 2014;27(9):1019–29. doi:10.1002/nbm.3147 [PubMed: 24913989]

33. Lin G, Zhuang C, Shen Z, et al. APT Weighted MRI as an Effective Imaging Protocol to Predict Clinical Outcome After Acute Ischemic Stroke. Original Research. Frontiers in Neurology. 2018-October-23 2018;9doi:10.3389/fneur.2018.00901

34. Dagher AP, Alertas AH, Choyke P, Balaban RS. Imaging of urea using chemical exchange dependent saturation transfer at 1.5T. J Magn Reson Im. 2000;12:745–748.

35. Ward KM, Aletras AH, Balaban RS. A new class of contrast agents for MRI based on proton chemical exchange dependent saturation transfer (CEST). J Magn Reson. Mar 2000;143(1):79–87. doi:10.1006/jmre.1999.1956 [PubMed: 10698648]

36. Ward KM, Balaban RS. Determination of pH using water protons and chemical exchange dependent saturation transfer (CEST). Magn Reson Med. Nov 2000;44(5):799–802. doi:Doi 10.1002/1522-2594(200011)44:5<799::Aid-Mrm18>3.0.Co;2-S [PubMed: 11064415]

37. Gao T, Zou C, Li YA-O, Jiang ZA-O, Tang X, Song XA-O. A Brief History and Future Prospects of CEST MRI in Clinical Non-Brain Tumor Imaging. LID - 10.3390/ijms222111559 [doi] LID - 11559. (1422–0067 (Electronic))

38. Schmitt B, Zamecnik P, Zaiss M, et al. A New Contrast in MR Mammography by Means of Chemical Exchange Saturation Transfer (CEST) Imaging at 3 Tesla: Preliminary Results. Rofo-Fortschritte Auf Dem Gebiet Der Rontgenstrahlen Und Der Bildgebenden Verfahren. Nov 2011;183(11):1030–1036. doi:10.1055/s-0031-1281764

39. Zhang S, Keupp J, Wang X, et al. Z-spectrum appearance and interpretation in the presence of fat: Influence of acquisition parameters. Magn Reson Med. May 2018;79(5):2731–2737. doi:10.1002/mrm.26900 [PubMed: 28862349]

40. Dula AN, Arlinghaus LR, Dortch RD, et al. Amide proton transfer imaging of the breast at 3 T: Establishing reproducibility and possible feasibility assessing chemotherapy response. Magn Reson Med. Jul 2013;70(1):216–224. doi:10.1002/mrm.24450 [PubMed: 22907893]

41. Klomp DWJ, Dula AN, Arlinghaus LR, et al. Amide proton transfer imaging of the human breast at 7T: development and reproducibility. NMR Biomed. Oct 2013;26(10):1271–1277. doi:10.1002/nbm.2947 [PubMed: 23559550]

42. Dula AN, Dewey BE, Arlinghaus LR, et al. Optimization of 7-T chemical exchange saturation transfer parameters for validation of glycosaminoglycan and amide proton transfer of fibroglandular breast tissue. Radiology. Apr 2015;275(1):255–61. doi:10.1148/radiol.14140762 [PubMed: 25353249]

43. Jones CK, Polders D, Hua J, et al. In vivo three-dimensional whole-brain pulsed steady-state chemical exchange saturation transfer at 7 T. Magn Reson Med. Jun 2012;67(6):1579–89. doi:10.1002/mrm.23141 [PubMed: 22083645]

44. Krikken E, Khlebnikov V, Zaiss M, et al. Amide chemical exchange saturation transfer at 7 T: a possible biomarker for detecting early response to neoadjuvant chemotherapy in breast cancer patients. Breast Cancer Res. Jun 14 2018;20(1):51. doi:10.1186/s13058-018-0982-2 [PubMed: 29898745]

45. Zhang S, Seiler S, Wang X, et al. CEST-Dixon for human breast lesion characterization at 3 T: A preliminary study. Magn Reson Med. Sep 2018;80(3):895–903. doi:10.1002/mrm.27079 [PubMed: 29322559]

46. Zimmermann F, Korzowski A, Breitling J, et al. A novel normalization for amide proton transfer CEST MRI to correct for fat signal–induced artifacts: application to human breast cancer imaging. 10.1002/mrm.27983. Magn Reson Med. 2020/03/01 2020;83(3):920–934. doi:10.1002/mrm.27983 [PubMed: 31532006]

47. Zaiss M, Xu J Fau - Goerke S, Goerke S Fau - Khan IS, et al. Inverse Z-spectrum analysis for spillover-, MT-, and T1 -corrected steady-state pulsed CEST-MRI--application to pH-weighted MRI of acute stroke. (1099–1492 (Electronic))

48. Loi L, Zimmermann F, Goerke S, et al. Relaxation-compensated CEST (chemical exchange saturation transfer) imaging in breast cancer diagnostics at 7T. Eur J Radiol. Aug 2020;129:109068. doi:10.1016/j.ejrad.2020.109068 [PubMed: 32574936]

49. Zaric O, Farr A, Poblador Rodriguez E, et al. 7T CEST MRI: A potential imaging tool for the assessment of tumor grade and cell proliferation in breast cancer. Magn Reson Imaging. Jun 2019;59(1873–5894 (Electronic)):77–87. doi:10.1016/j.mri.2019.03.004 [PubMed: 30880110]

50. Meng N, Wang X, Sun J, et al. A comparative study of the value of amide proton transfer-weighted imaging and diffusion kurtosis imaging in the diagnosis and evaluation of breast cancer. Eur Radiol. Mar 2021;31(3):1707–1717. doi:10.1007/s00330-020-07169-x [PubMed: 32888071]

51. Dula AN, Arlinghaus LR, Dortch RD, et al. Amide proton transfer imaging of the breast at 3 T: establishing reproducibility and possible feasibility assessing chemotherapy response. Magn Reson Med. Jul 2013;70(1):216–24. doi:10.1002/mrm.24450 [PubMed: 22907893]

52. Nishie A, Takayama Y, Asayama Y, et al. Amide proton transfer imaging can predict tumor grade in rectal cancer. Magn Reson Imaging. Sep 2018;51:96–103. doi:10.1016/j.mri.2018.04.017 [PubMed: 29729438]

53. Takayama Y, Nishie A, Togao O, et al. Amide Proton Transfer MR Imaging of Endometrioid Endometrial Adenocarcinoma: Association with Histologic Grade. Radiology. Mar 2018;286(3):909–917. doi:10.1148/radiol.2017170349 [PubMed: 29083987]

54. Zhang S, Rauch GM, Adrada BE, et al. Assessment of Early Response to Neoadjuvant Systemic Therapy in Triple-Negative Breast Cancer Using Amide Proton Transfer-weighted Chemical Exchange Saturation Transfer MRI: A Pilot Study. Radiol Imaging Cancer. Sep 2021;3(5):e200155. doi:10.1148/rycan.2021200155 [PubMed: 34477453]

55. Liu Z, Wen J, Wang M, et al. Breast Amide Proton Transfer Imaging at 3 T: Diagnostic Performance and Association With Pathologic Characteristics. J Magn Reson Im. 2022;doi:10.1002/jmri.28335

56. Loi L, Goerke S, Zimmermann F, et al. Assessing the influence of the menstrual cycle on APT CEST-MRI in the human breast. Magn Reson Imaging. 2022/09/01/ 2022;91:24–31. doi:10.1016/j.mri.2022.05.006 [PubMed: 35550841]

57. Donahue MJ, Donahue PC, Rane S, et al. Assessment of lymphatic impairment and interstitial protein accumulation in patients with breast cancer treatment-related lymphedema using CEST MRI. Magn Reson Med. Jan 2016;75(1):345–55. doi:10.1002/mrm.25649 [PubMed: 25752499]

58. Crescenzi R, Donahue PMC, Mahany H, Lants SK, Donahue MJ. CEST MRI quantification procedures for breast cancer treatment-related lymphedema therapy evaluation. 10.1002/mrm.28031. Magn Reson Med. 2020/05/01 2020;83(5):1760–1773. doi:10.1002/mrm.28031 [PubMed: 31631410]

59. Chan KW, Jiang L, Cheng M, et al. CEST-MRI detects metabolite levels altered by breast cancer cell aggressiveness and chemotherapy response. NMR Biomed. Jun 2016;29(6):806–16. doi:10.1002/nbm.3526 [PubMed: 27100284]

60. Mancini L, Casagranda S, Gautier G, et al. CEST MRI provides amide/amine surrogate biomarkers for treatment-naïve glioma sub-typing. Eur J Nucl Med Mol Imaging. Jun 2022;49(7):2377–2391. doi:10.1007/s00259-022-05676-1 [PubMed: 35029738]

61. Keupp J, Togao O. Magnetization transfer ratio based metric for APTw or CESTw MRI suppressing signal from fluid compartments - initial application to glioblastoma assessmen. 2018:

62. Jia G, Abaza R, Williams JD, et al. Amide proton transfer MR imaging of prostate cancer: a preliminary study. Article. J Magn Reson Imaging. Mar 2011;33(3):647–54. doi:10.1002/jmri.22480 [PubMed: 21563248]

63. Takayama Y, Nishie A, Sugimoto M, et al. Amide proton transfer (APT) magnetic resonance imaging of prostate cancer: comparison with Gleason scores. MAGMA. Aug 2016;29(4):671–9. doi:10.1007/s10334-016-0537-4 [PubMed: 26965511]

64. Kasivisvanathan V, Rannikko AS, Borghi M, et al. MRI-Targeted or Standard Biopsy for Prostate-Cancer Diagnosis. New Engl J Med. 2018/05/10 2018;378(19):1767–1777. doi:10.1056/NEJMoa1801993 [PubMed: 29552975]

65. Yin H, Wang D, Yan R, et al. Comparison of Diffusion Kurtosis Imaging and Amide Proton Transfer Imaging in the Diagnosis and Risk Assessment of Prostate Cancer. Front Onc. 2021;11:640906–640906. doi:10.3389/fonc.2021.640906

66. Chen S-Z, Yuan J, Deng M, Wei J, Zhou J, Wáng Y-XJ. Chemical exchange saturation transfer (CEST) MR technique for in-vivo liver imaging at 3.0 tesla. Eur Radiol. 2016;26(6):1792–1800. doi:10.1007/s00330-015-3972-0 [PubMed: 26334509]

67. Deng M, Chen SZ, Yuan J, Chan Q, Zhou J, Wang YX. Chemical Exchange Saturation Transfer (CEST) MR Technique for Liver Imaging at 3.0 Tesla: an Evaluation of Different Offset Number and an After-Meal and Over-Night-Fast Comparison. Article. Mol Imaging Biol. Apr 2016;18(2):274–82. doi:10.1007/s11307-015-0887-8 [PubMed: 26391991]

68. Tang Y, Xiao G, Shen Z, et al. Noninvasive Detection of Extracellular pH in Human Benign and Malignant Liver Tumors Using CEST MRI. 10.3389/fonc.2020.578985. Front Onc. 2020;10:2349.

69. Chen MM, Chen CY, Shen ZW, et al. Extracellular pH is a biomarker enabling detection of breast cancer and liver cancer using CEST MRI. Oncotarget. Jul 11 2017;8(28):45759–45767. doi:10.18632/oncotarget.17404 [PubMed: 28501855]

70. Seo N, Jeong HK, Choi JY, Park MS, Kim MJ, Chung YE. Liver MRI with amide proton transfer imaging: feasibility and accuracy for the characterization of focal liver lesions. Eur Radiol. Jan 2021;31(1):222–231. doi:10.1007/s00330-020-07122-y [PubMed: 32785767]

71. Nishie A, Asayama Y, Ishigami K, et al. Amide proton transfer imaging to predict tumor response to neoadjuvant chemotherapy in locally advanced rectal cancer. 10.1111/jgh.14315. J Gastroenterol Hepatol. 2019/01/01 2019;34(1):140–146. doi:10.1111/jgh.14315 [PubMed: 29900583]

72. Li L, Chen W, Yan Z, et al. Comparative Analysis of Amide Proton Transfer MRI and Diffusion-Weighted Imaging in Assessing p53 and Ki-67 Expression of Rectal Adenocarcinoma. J Magn Reson Imaging. Nov 2020;52(5):1487–1496. doi:10.1002/jmri.27212 [PubMed: 32524685]

73. Chen W, Li L, Yan Z, et al. Three-dimension amide proton transfer MRI of rectal adenocarcinoma: correlation with pathologic prognostic factors and comparison with diffusion kurtosis imaging. Eur Radiol. May 2021;31(5):3286–3296. doi:10.1007/s00330-020-07397-1 [PubMed: 33125558]

74. Li J, Lin L, Gao X, Li S, Cheng J. Amide Proton Transfer Weighted and Intravoxel Incoherent Motion Imaging in Evaluation of Prognostic Factors for Rectal Adenocarcinoma. Front Oncol. 2021;11:783544. doi:10.3389/fonc.2021.783544 [PubMed: 35047400]

75. Ohno Y, Yui M, Koyama H, et al. Chemical Exchange Saturation Transfer MR Imaging: Preliminary Results for Differentiation of Malignant and Benign Thoracic Lesions. Radiology. 2016/05/01 2015;279(2):578–589. doi:10.1148/radiol.2015151161 [PubMed: 26588021]

76. Luo J, Abaci Turk E, Gagoski B, et al. Preliminary evaluation of dynamic glucose enhanced MRI of the human placenta during glucose tolerance test. Quant Imaging Med Surg. Oct 2019;9(10):1619–1627. doi:10.21037/qims.2019.09.16 [PubMed: 31728306]

77. Abergel D, Palmer AGI. On the use of the stochastic Liouville equation in nuclear magnetic resonance: application to R1r relaxation in the presence of exchange. Concepts in Magnetic Resonance A. 2003;19:134–148.

78. Walker-Samuel S, Ramasawmy R, Torrealdea F, et al. In vivo imaging of glucose uptake and metabolism in tumors. Nat Med. Aug 2013;19(8):1067–72. doi:10.1038/nm.3252 [PubMed: 23832090]

79. Cai K, Xu HN, Singh A, et al. Breast cancer redox heterogeneity detectable with chemical exchange saturation transfer (CEST) MRI. Mol Imaging Biol. Oct 2014;16(5):670–9. doi:10.1007/s11307-014-0739-y [PubMed: 24811957]

80. Li B, Sun H, Zhang S, Wang X, Guo Q. The utility of APT and IVIM in the diagnosis and differentiation of squamous cell carcinoma of the cervix: A pilot study. Magn Reson Imaging. 2019/11/01 2019;63:105–113. doi:10.1016/j.mri.2019.08.020 [PubMed: 31425797]

81. He Y-L, Li Y, Lin C-Y, et al. Three-dimensional turbo-spin-echo amide proton transfer-weighted mri for cervical cancer: A preliminary study. 10.1002/jmri.26710. J Magn Reson Im. 2019/10/01 2019;50(4):1318–1325. doi:10.1002/jmri.26710

82. Li B, Sun H, Zhang S, Wang X, Guo Q. Amide proton transfer imaging to evaluate the grading of squamous cell carcinoma of the cervix: A comparative study using (18) F FDG PET. J Magn Reson Imaging. Jul 2019;50(1):261–268. doi:10.1002/jmri.26572 [PubMed: 30430677]

83. Longo DL, Dastru W, Digilio G, et al. Iopamidol as Responsive MRI-Chemical Exchange Saturation Transfer Contrast Agent for pH Mapping of Kidneys: In Vivo Studies in Mice at 7T. Magn Reson Med. 2011;65:202–211. [PubMed: 20949634]

84. Longo DL, Busato A, Lanzardo S, Antico F, Aime S. Imaging the pH evolution of an acute kidney injury model by means of iopamidol, a MRI-CEST pH-responsive contrast agent. Magn Reson Med. Sep 2013;70(3):859–64. doi:10.1002/mrm.24513 [PubMed: 23059893]

85. Jones KM, Randtke EA, Yoshimaru ES, et al. Clinical Translation of Tumor Acidosis Measurements with AcidoCEST MRI. Mol Imaging Biol. Aug 2017;19(4):617–625. doi:10.1007/s11307-016-1029-7 [PubMed: 27896628]

86. Sun PZ, Zhou J, Sun W, Huang J, van Zijl PC. Suppression of lipid artifacts in amide proton transfer imaging. Magn Reson Med. Jul 2005;54(1):222–5. doi:10.1002/mrm.20530 [PubMed: 15968669]

87. Dixon WT. Simple proton spectroscopic imaging. Radiology. Oct 1984;153(1):189–94. doi:10.1148/radiology.153.1.6089263 [PubMed: 6089263]

88. Glover GH. Multipoint Dixon technique for water and fat proton and susceptibility imaging. J Magn Reson Imaging. Sep-Oct 1991;1(5):521–30. doi:10.1002/jmri.1880010504 [PubMed: 1790376]

89. Reeder SB, Pineda AR, Wen Z, et al. Iterative decomposition of water and fat with echo asymmetry and least-squares estimation (IDEAL): application with fast spin-echo imaging. Magn Reson Med. Sep 2005;54(3):636–44. doi:10.1002/mrm.20624 [PubMed: 16092103]

90. Ma J. Dixon techniques for water and fat imaging. J Magn Reson Imaging. Sep 2008;28(3):543–58. doi:10.1002/jmri.21492 [PubMed: 18777528]

91. Ma J, Son JB, Zhou Y, Le-Petross H, Choi H. Fast spin-echo triple-echo dixon (fTED) technique for efficient T2-weighted water and fat imaging. 10.1002/mrm.21268. Magn Reson Med. 2007/07/01 2007;58(1):103–109. doi:10.1002/mrm.21268 [PubMed: 17659631]

92. Wang X, Hernando D, Reeder SB. Sensitivity of chemical shift-encoded fat quantification to calibration of fat MR spectrum. Magn Reson Med. 2016;75(2):845–851. doi:10.1002/mrm.25681 [PubMed: 25845713]

93. Zhao Y, Yan X, Zhang Z, Zhao W, Liu Z, Li J. Self-adapting multi-peak water-fat reconstruction for the removal of lipid artifacts in chemical exchange saturation transfer (CEST) imaging. 10.1002/mrm.27859. Magn Reson Med. 2019/11/01 2019;82(5):1700–1712. doi: [PubMed: 31241219]

94. Sun PZ. Development of intravoxel inhomogeneity correction for chemical exchange saturation transfer spectral imaging: a high-resolution field map-based deconvolution algorithm for magnetic field inhomogeneity correction. Magn Reson Med. 2020;83(4):1348–1355. doi:10.1002/mrm.28015 [PubMed: 31628765]

95. Ng M-C, Hua J, Hu Y, Luk K, Lam E. Magnetization Transfer (MT) Assymetry Around Water Resonance in Human Cervical Spinal Cord Journal of Magnetic Resonance. 2009;29:523–528.

96. Schmitt B, Zamecnik P, Zaiss M, et al. A new contrast in MR mammography by means of chemical exchange saturation transfer (CEST) imaging at 3 Tesla: preliminary results. Rofo. Nov 2011;183(11):1030–6. doi:10.1055/s-0031-1281764 [PubMed: 22034086]

97. Bernstein MA, King KF, Zhou XJ. Handbook of MRI pulse sequences. Elsevier Academic Press; 2004.

98. Kim M, Gillen J, Lamndman B, Zhou JY, van Zijl PCM. Water suppression shift referencing (WASSR) for chmical exchange saturation transfer (CEST) experiments. Magn Reson Med. 2009;61(6):1441–1450. [PubMed: 19358232]

99. Schuenke P, Windschuh J, Roeloffs V, Ladd ME, Bachert P, Zaiss M. Simultaneous mapping of water shift and B1(WASABI)—Application to field-Inhomogeneity correction of CEST MRI data. 10.1002/mrm.26133. Magn Reson Med. 2017/02/01 2017;77(2):571–580. doi:10.1002/mrm.26133 [PubMed: 26857219]

100. Windschuh J, Zaiss M, Meissner JE, et al. Correction of B1-inhomogeneities for relaxation-compensated CEST imaging at 7 T. NMR Biomed. May 2015;28(5):529–37. doi:10.1002/nbm.3283 [PubMed: 25788155]

101. Phillip Zhe S, Iris Yuewen Z, Takahiro I, Yingkun G, Gang X, Renhua W. Simplified correction of B1 inhomogeneity for chemical exchange saturation transfer (CEST) MRI measurement with surface transceiver coil. 2015:

102. Robson PM, Madhuranthakam AJ, Dai W, Pedrosa I, Rofsky NM, Alsop DC. Strategies for Reducing Respiaratory Motion Artifacts in Renal Perfusion Imaging with Arterial Spin Labeling. Magn Reson Med. 2009;61(6):1374–1487. [PubMed: 19319891]

103. Wech TA-O, Köstler HA-O. Robust motion correction in CEST imaging exploiting low-rank approximation of the z-spectrum. (1522–2594 (Electronic))

104. Heo HY, Zhang Y, Lee DH, Jiang S, Zhao X, Zhou J. Accelerating chemical exchange saturation transfer (CEST) MRI by combining compressed sensing and sensitivity encoding techniques. Article. Magn Reson Med. Feb 2017;77(2):779–786. doi:10.1002/mrm.26141 [PubMed: 26888295]

105. Heo HY, Xu X, Jiang S, et al. Prospective acceleration of parallel RF transmission-based 3D chemical exchange saturation transfer imaging with compressed sensing. 10.1002/mrm.27875. Magn Reson Med. Nov 2019;82(5):1812–1821. doi:10.1002/mrm.27875 [PubMed: 31209938]

106. She H, Greer JS, Zhang S, et al. Accelerating chemical exchange saturation transfer MRI with parallel blind compressed sensing. Magn Reson Med. Jan 2019;81(1):504–513. doi:10.1002/mrm.27400 [PubMed: 30146714]

107. Perlman O, Zhu B, Zaiss M, Rosen MS, Farrar CT. An end-to-end AI-based framework for automated discovery of rapid CEST/MT MRI acquisition protocols and molecular parameter quantification (AutoCEST). Magn Reson Med. 2022;87(6):2792–2810. doi:10.1002/mrm.29173 [PubMed: 35092076]

108. Herz K, Mueller S, Perlman O, et al. Pulseq-CEST: Towards multi-site multi-vendor compatibility and reproducibility of CEST experiments using an open-source sequence standard. Magn Reson Med. Oct 2021;86(4):1845–1858. doi:10.1002/mrm.28825 [PubMed: 33961312]

109. Yao J, Wang C, Raymond C, et al. A physical phantom for amine chemical exchange saturation transfer (CEST) MRI. MAGMA. 2021/08/01 2021;34(4):569–580. doi:10.1007/s10334-020-00902-z [PubMed: 33484366]
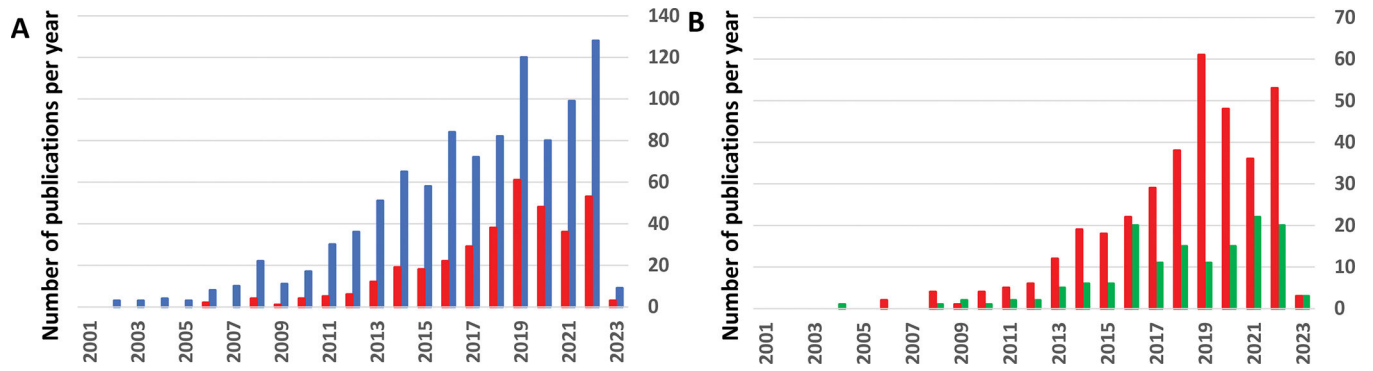
Figure 1.
SCOPUS publication search results for **A:** overall CEST (using search string "(CEST or APTw) and MRI", blue), vs neuro CEST (search string "(CEST or APTw) and MRI and (neuro or brain)", red); **B:** neuro CEST (search string "(CEST or APTw) and MRI and (neuro or brain)", red) vs body CEST (search string (CEST or APTw) and MRI and (breast or renal or kidney or prostate or liver or rectum or lung), green). Publication years starting with 2000.
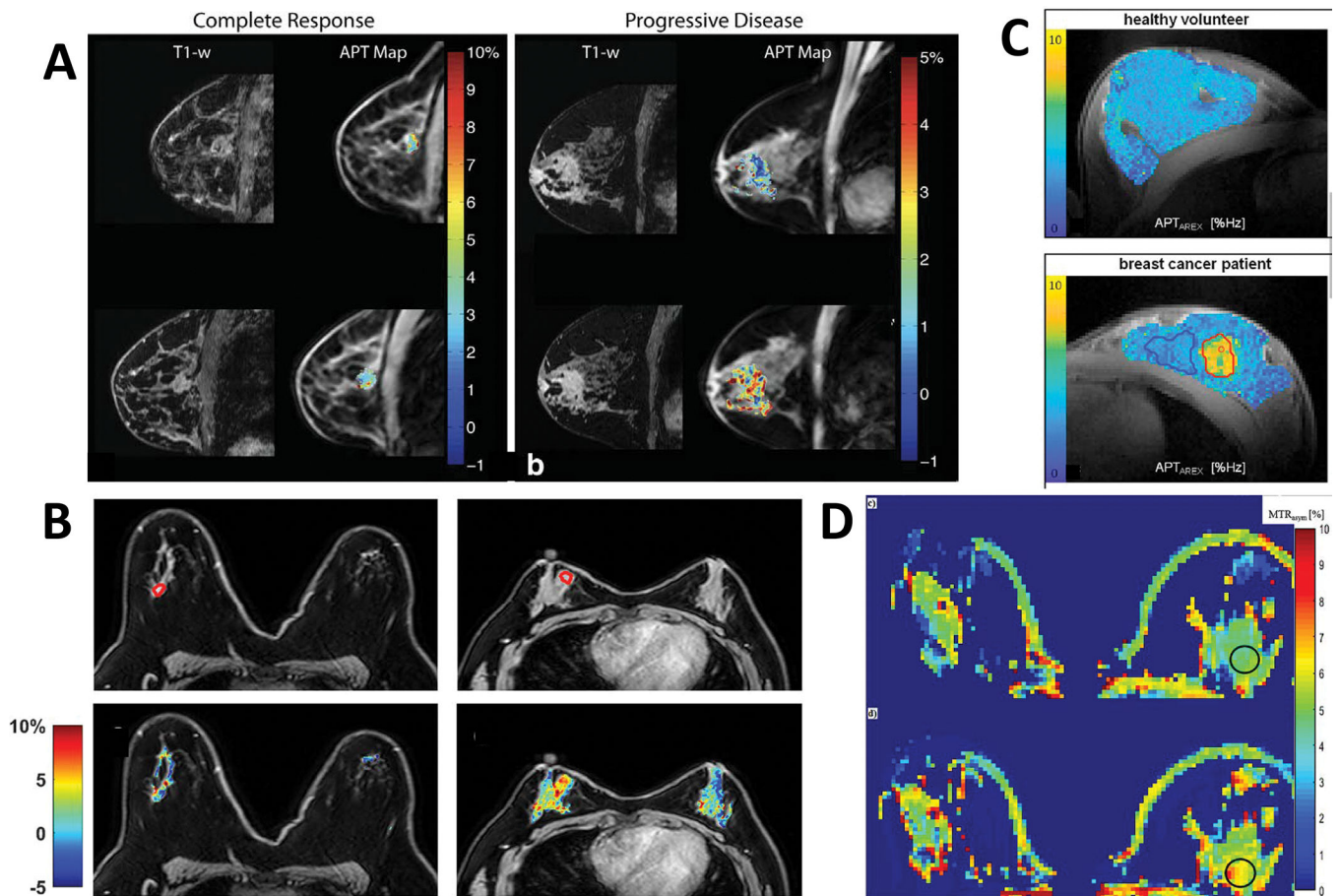
Figure 2.
Examples of CEST maps in breast cancer studies. **A:** overlay of tumor APT maps on corresponding anatomical images before (upper panels and after (bottom panels) one cycle of neoadjuvant chemotherapy for a patient achieving complete response (left panels) and a patient with progressive disease (right panels). *Reprinted with permission from Ref.*[51]. **B:** Anatomical water only images (top panels) and hydroxyl CEST maps (bottom panels) of Invasive Ductal Carcinoma, not otherwise specified, patient (left) and a triple-negative breast cancer patient (right). ROI on anatomical images mark the tumors. *Reprinted with permission from Ref.*[45]. **C:** APT$_{AREX}$ map of a representative breast cancer IDC patient (cancer lesion red ROI, bottom panel) and a healthy volunteer (top panel). *Reprinted with permission from Ref.* [48]. **D:** The CEST map calculated at 1.4 ppm (top panel) and 3.5 ppm (bottom panel). *Reprinted with permission from Ref.*[49].
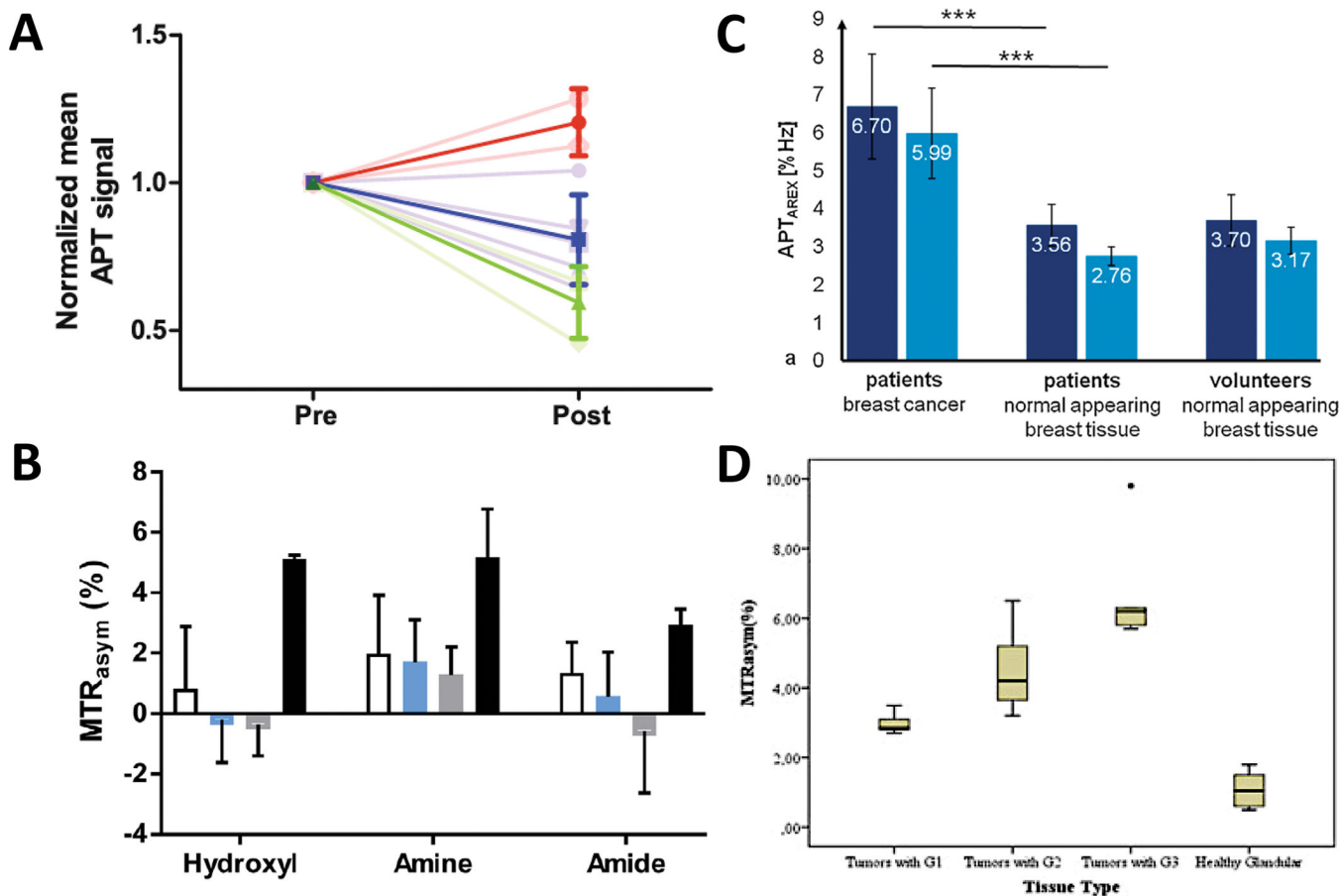
Figure 3.
Examples of CEST correlation with therapy response (A) or cancer aggressiveness (B-D) in human breast cancer studies. **A**: Normalized changes in APT after the first cycle of neoadjuvant chemotherapy in the slice with the largest tumor diameter. The mean of the non-responders (bright red line), partial responders (bright blue line), and complete responders (bright green line) on top of the change in APT signal of all the lesions (transparent lines in the background), where each line represents a different lesion. The standard deviation in each group is shown as error bars. *Reprinted from Ref.*[44] *under Creative Commons Attribution 4.0 International License (*http://creativecommons.org/licenses/by/4.0/*).* **B:** The MTR$_{asym}$ averaged in three frequency ranges for normal (white), benign (blue), estrogen receptor (ER) positive (ER+, gray) and ER- (black) Invasive Ductal Carcinoma (IDC) groups. *Reprinted with permission from Ref.*[45]. **C:** Mean conventional (light blue) and fat-corrected (dark blue) APT$_{AREX}$ in breast cancer lesions vs normal-appearing fibroglandular tissue in volunteers and patients (***, p<0.001) *Reprinted with permission from Ref.*[48]. **D.** Boxplot diagram of maximal values of MTR$_{asym}$ from breast cancer lesions (divided into three groups based on grade 1, 2, and 3 (G1, G2, and G3)) and for normal appearing fibroglandular tissues from the contralateral side. *Reprinted with permission from Ref*[49].
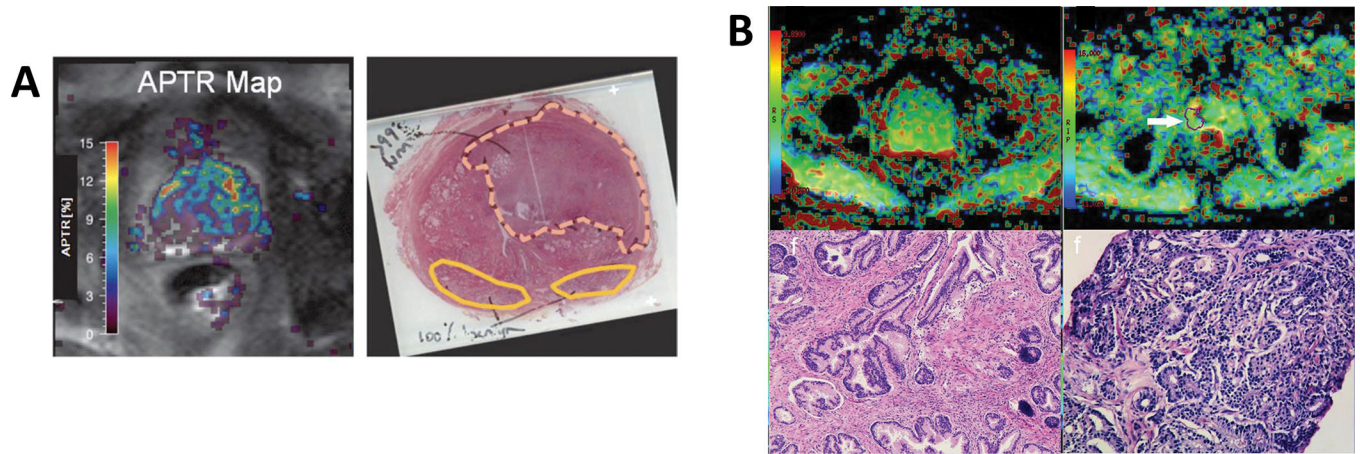
Figure 4.
Examples of CEST studies in prostate cancer. **A:** APT map (left panel) for a case with a Transition Zone (TZ) tumor (Gleason score: 3 + 4 = 7, pathologic stage: T3b). The pathologic slide (right panel) shows the tumor region (yellow dashed line) and two Peripheral Zone (PZ) benign regions (yellow solid line). *Reprinted with permission from Ref.* [62]. **B:** APT pseudo-colored maps (top panels) and pathological images (bottom panels) of BPH case (left panels) and GS=8 prostate cancer (right panels, arrow). *Reprinted from Ref.* [65] *under Creative Commons Attribution 4.0 International License* (http://creativecommons.org/licenses/by/4.0/).
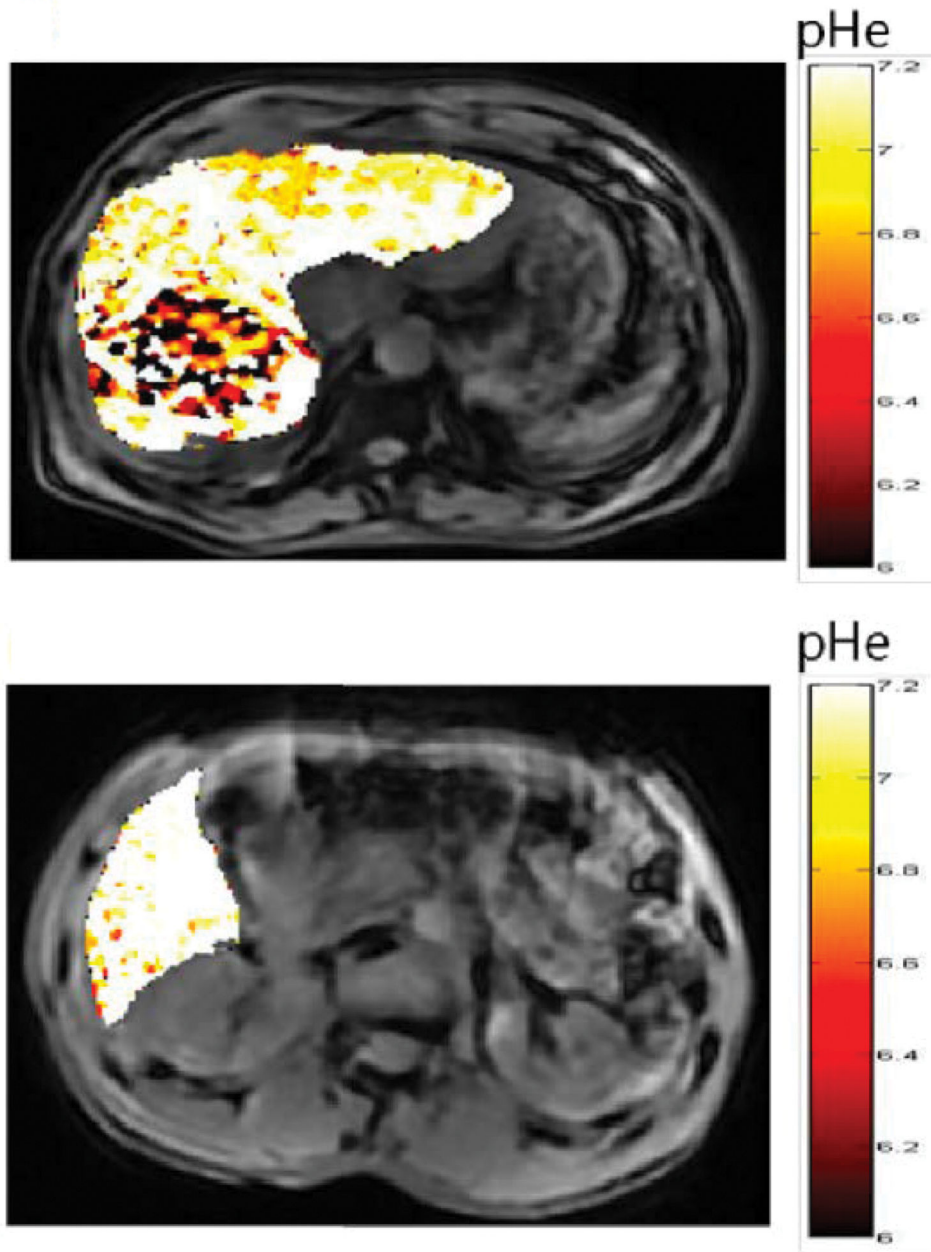
Figure 5.
Example of CEST studies in liver. pHe values maps of hepatic carcinoma (left panel) and hepatic hemangioma (right panel) quantified using dual-power CEST-MRI and exogenous agent Ioversol. *Reprinted from Ref.* [68] *under Creative Commons Attribution 4.0 International License (*http://creativecommons.org/licenses/by/4.0/*).*
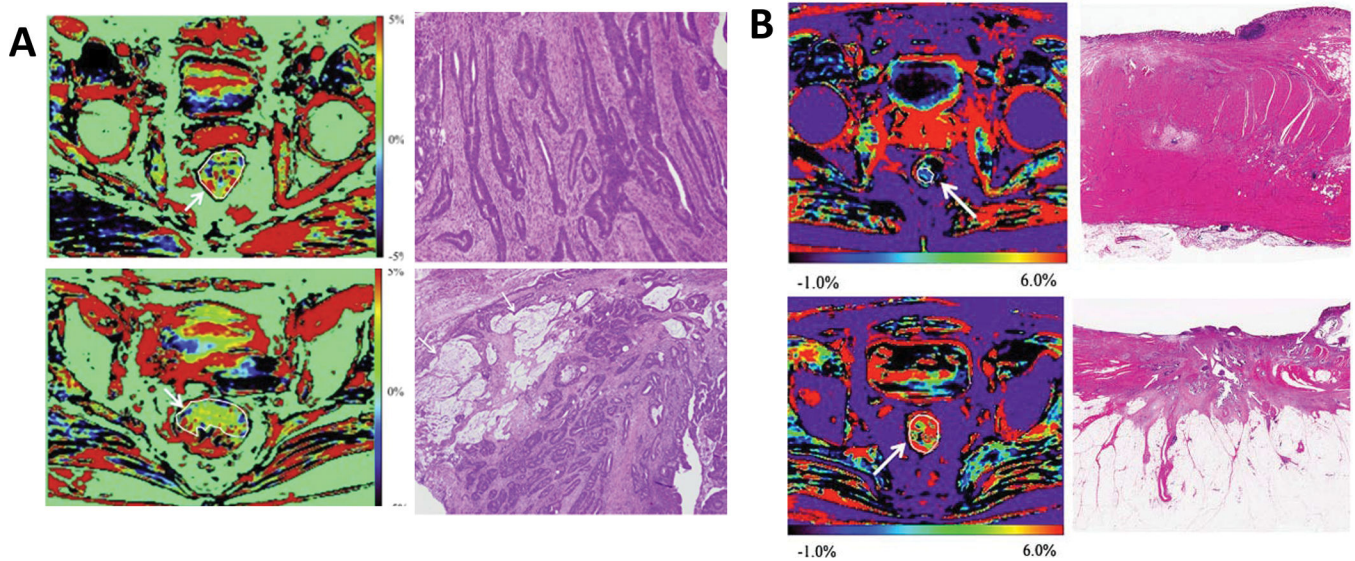
Figure 6.
Examples of CEST studies of rectal cancer. **A:** The APTw maps (left panels) and H. E. staining (right panels) for patients with well differentiated adenocarcinoma (top panel) and moderately differentiated adenocarcinoma including high mucinous components (bottom panel). A region-of-interest placed over tumor is also shown (arrows). *Reprinted with permission from Ref.* [52]. **B:** Imaging of patient withs rectal cancer resected after three courses of XEROX (capecitabine and oxaliplatin). The APTw maps (left panels) and H.E. staining (right panels). The degree of histological degeneration and necrosis was Grade 3 (top panels) and Grade 1 (bottom panels) on HE staining. Arrows on APT maps show region-of-interests for quantitative measurements. Case at the top panels demonstrates complete necrosis, while residual tumors are observed in the case at the bottom panels (arrows on H.E. staining). *Reprinted with permission from Ref.* [71].
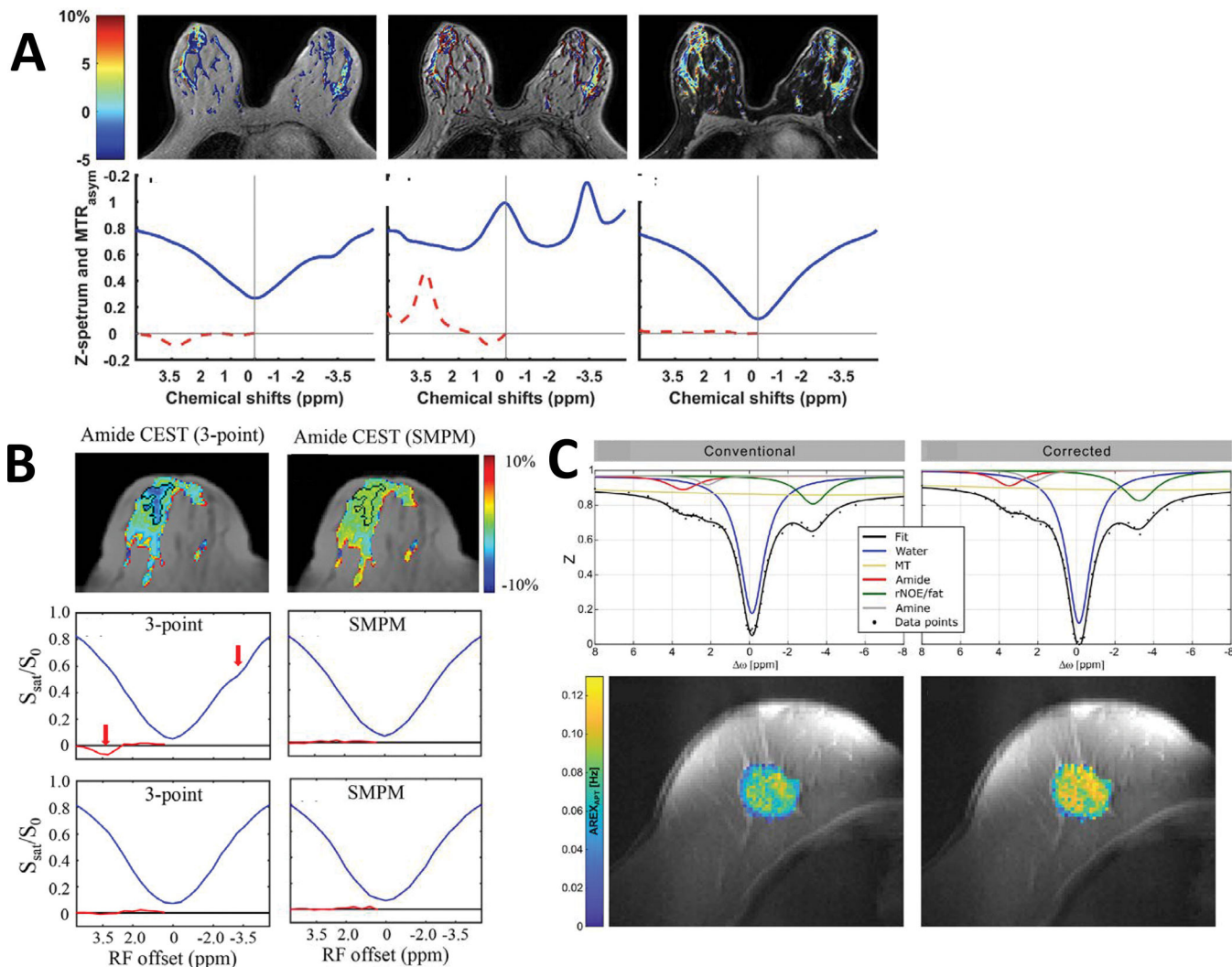
Figure 7.
Lipid influence on CEST signal and proposed solutions. **A:** APT maps (top panels), the corresponding Z-spectra and MTR_{asym} (bottom row) from region of interest (ROI) encompassing all fibroglandular tissue obtained with (right-most panels) and without Dixon (left-most and middle panels). The non-Dixon and Dixon images refer to the second echo source image (left-most panels) or first echo source image (middle panels) and water-only image (right-most panels). *Reprinted pending permission from Ref.* [45]. **B:** APT maps (top row) reconstructed using three-point mDixon (left panels) and self-adapting multi-peak model (SMPM, right panels), the corresponding Z-spectrum (blue line) and MTRasym (red line) of two pixels in a high fat fraction region (middle row) and a low fat-fraction region (bottom row). *Reprinted with permission from Ref.* [93]. **C:** APT_{AREX} image (bottom row) of a patient with invasive mucinous mamma carcinoma (G2). Conventional (left panels) and fat signal–corrected (right panels) Z-spectra ($B_1 = 0.6$ μT, top row) of an exemplary voxel within the tumor. *Reprinted with permission from Ref.* [46].

Table 1.

Selection of saturation parameters and correction methods in CEST studies of breast cancer patients

Publication	Number of controls/ patients	Field	Each pulse dur (msec)	Number of pulses	Total Saturation length (msec)	B_1 or B_1^+ (μT)	DC	Fat Suppression	Acq Type	Number of slices	Frequency span/ increment (ppm)	Total Acq length m:s	B_0 correction
Schmitt, et.al., 2011 [38]	6/6	3T	100	5	1000	1.5	50%	None	3D SPGR		±4 /0.667		Minimum of Z spectrum
Dula, et.al., 2013 [40]	10/3	3T	25	35	962.5	0.5	91%	Binomial (1–3–3–1) pulse	3D TFE	10	±6 /0.3	6:42	Single Lor fit
Klomp, et.al., 2013 [41]	6/0	7T	10	200	2000.0	1 *	50%	Water-selective binomial (1–2–1) pulse	Multi-shot 3D TFE	12	−5÷9 /0.25 *	5:00	Single Lor Fit
Dula, et.al., 2015 [42]	10/0	7T	25	Steady-state 3D		1		Water selective binomial pulse	Multi-shot 3D TFE	12	±40 / 1.8 *		Single Lor
Krikken, et.al., 2018 [44]	0/9	7T	100	20	4000.0	2	50%	1–2–1 Spectral Spatial pulse	Multi-shot 3D TFE			4:55	WASSR
Zhang, et.al., 2018 [39]	0/10	3T	49.5	10	500	1.2	99%	mDixon	2D mDixon TFE	1	±6 / 0.375	2:26	mDixon B_0
Zimmerman, et.al., 2019[46]**& Loi, et.al., 2019**[48]	1/2 & 7/10	7T	15	297	5600	0.6 and 0.9	80%	Novel normalization	2D ss-TFE		Unequal *	4:20 / slice	WASSABI
Zaric, et.al., 2019 [49]	9/18	7T	50	8		1 #	80%	Water selective binomial pulse	3D multi-shot GRE	30	±4 / 0.267	13:30	Minimum of Z spectrum *
Meng, et.al., 2021 [50]	0/133	3T	500	4	2000	2	100%	STIR	EPI	as needed	±4.7/0.2 *		
Zhang, et.al., 2021[50,54]	0/51	3T	0.232	6250 for 0.93571 for 2.0	3500 for 0.92000 for 2.0	0.9 and 2.0	41%	Fat saturation pulses	ss-TSE	1	±7/0.5	4:18 &	WASSR
Donahue, et.al., 2016 [57]	8/7	3T	75	Steady-state 3D		1			Multi-shot 3D EPI	20	±6/0.25		Single Lor fit
Liu, et.al., 2022 [55]	0/103 (84)	3T	0.232		2000	2	50%	CHESS	ss-TSE	1	±7/0.5	4:30	WASSR
Crescenzi, et.al., 2019 [58]	17/12	3T	75	Steady-state 3D		2			EPI	9	Asymmetric *	6:00	Minimum of Z spectrum

* For additional details and/or parameters see the original manuscript cited.

Mean

& CEST+WASSR;

TFE (turbo field echo) = fast segmented GRE;

TSE(turbo spin echo) = fast multi-echo SE

TSE(turbo spin echo) = fast multi-echo SE

ss=single shot

Table 2.

Selection of saturation parameters and correction methods in CEST studies other than breast

Body area	Publication	Number of control / patients	Field	Each pulse dur (msec)	Number of pulses	Total Saturation length (msec)	B_1 or B_1^+ (µT)	DC	Fat Suppression	Acq Type	Number of slices	Frequency span/ increment (ppm)	Total Acq length min:se
Prostate	**Jia, et.al., 2011** [62]	0/12	3T	31	16	496	3.8	100%		ss-TSE	1	±8 / 0.5	3:56
	Takayama, et.al., 2016 [63]	0/170(66)	3T	50	10	500	2	100%		ss-TSE	1	±6 / 0.5	2:20
	Yin, et.al., 2021 [65]	0/129(100)	3T	500	1	500	2	100%		ss-EPI	1	±4.7/ 0.2	2:36
Liver	**Chen, et.al., 2016** [66] **& Deng, et.al., 2016** [67]	8/0 & 15/0	3T	300	1	300	3	100%	CHESS	TSE	1	±5 / 0.25 &±5/ 0.25 *	4:58
	Tang, et.al., 2020 [68]	0/20	3T	28			0.2 & 1.15 *			GRE		±5 / 0.2	13:30
	Seo, et.al., 2021 [70]	0/203(79)	3T	200	4	800	1	100%	Yes	TSE	1	±2.72, ±3.5, ±4.28	~1:00
Rectum	**Nishie, et.al., 2018** [52] **& Nishie, et.al., 2019** [71]	0/20 & 0/17	3T	50	10	500	2	100%		TSE	1	±6 / 0.5	
	Li, et.al., 2020 [72] **& Chen, et.al., 2021** [73]	0/87(43) & 0/97(61)	3T			2000		100%	SPIR	TSE	6	+3.5, −3.5, +3.5±0.8	4:30
	Li, et.al., 2021 [74]	0/158(110)	3T	500	4	2000	2	100%	Yes	3D TSE	9	± 3.5, ± 3.42, ± 3.58	6:00
Thorax	**Ohno, et.al., 2016** [75]	0/21	3T	40	10	400	1–2	100%		TSE	1	±10/0.5	~10:00
Uterus (Endometrium)	**Takayama, et al., 2018** [53]	0/56(32) **	3T	50	10	500	2	100%		ss-TSE	1	±6 / 0.5	2:20
Uterus (Placenta)	**Luo, et.al., 2019** [76]	5/0	3T	1000	1	1000	1.5	100%		EPI		±5 / 0.2 Varying density for DGE *	DGE: 1:16
Cervix	**He, et.al., 2019** [81]	49/75(52)	3T	500	4	2000	2	100%	SPIR	3D TSE	9	+3.5, −3.5, +3.5±0.8	7:33
	Li, et.al., 2019 [80] **&**	20/69(32) & 0/81(31) **	3T	500	4	2000	2	100%	SPIR	3D TSE	9	+3.5, −3.5, +3.5±0.8, −3.5±1.6	5:46

Body area	Publication	Number of control / patients	Field	Each pulse dur (msec)	Number of pulses	Total Saturation length (msec)	B_1 or B_1^+ (µT)	DC	Fat Suppression	Acq Type	Number of slices	Frequency span/ increment (ppm)	Total Acq length min:se
	Li, et.al., 2019[82]												

*
For additional details and/or parameters see the original manuscript cited.

TFE (turbo field echo)=fast segmented GRE;

TSE(turbo spin echo)=fast multi-echo SE;

ss=single shot

**
Number in parenthesis is the number of patients in the final analysis vs number of patients enrolled in the study